NASA/TM—2003–212692

Correlation of Radiation Dosage With Mechanical Properties of Thin Films

R.L. Newton
Marshall Space Flight Center, Marshall Space Flight Center, Alabama

August 2003

The NASA STI Program Office...in Profile

Since its founding, NASA has been dedicated to the advancement of aeronautics and space science. The NASA Scientific and Technical Information (STI) Program Office plays a key part in helping NASA maintain this important role.

The NASA STI Program Office is operated by Langley Research Center, the lead center for NASA's scientific and technical information. The NASA STI Program Office provides access to the NASA STI Database, the largest collection of aeronautical and space science STI in the world. The Program Office is also NASA's institutional mechanism for disseminating the results of its research and development activities. These results are published by NASA in the NASA STI Report Series, which includes the following report types:

- TECHNICAL PUBLICATION. Reports of completed research or a major significant phase of research that present the results of NASA programs and include extensive data or theoretical analysis. Includes compilations of significant scientific and technical data and information deemed to be of continuing reference value. NASA's counterpart of peer-reviewed formal professional papers but has less stringent limitations on manuscript length and extent of graphic presentations.

- TECHNICAL MEMORANDUM. Scientific and technical findings that are preliminary or of specialized interest, e.g., quick release reports, working papers, and bibliographies that contain minimal annotation. Does not contain extensive analysis.

- CONTRACTOR REPORT. Scientific and technical findings by NASA-sponsored contractors and grantees.

- CONFERENCE PUBLICATION. Collected papers from scientific and technical conferences, symposia, seminars, or other meetings sponsored or cosponsored by NASA.

- SPECIAL PUBLICATION. Scientific, technical, or historical information from NASA programs, projects, and mission, often concerned with subjects having substantial public interest.

- TECHNICAL TRANSLATION. English-language translations of foreign scientific and technical material pertinent to NASA's mission.

Specialized services that complement the STI Program Office's diverse offerings include creating custom thesauri, building customized databases, organizing and publishing research results...even providing videos.

For more information about the NASA STI Program Office, see the following:

- Access the NASA STI Program Home Page at ***http://www.sti.nasa.gov***

- E-mail your question via the Internet to help@sti.nasa.gov

- Fax your question to the NASA Access Help Desk at (301) 621–0134

- Telephone the NASA Access Help Desk at (301) 621–0390

- Write to:
  NASA Access Help Desk
  NASA Center for AeroSpace Information
  7121 Standard Drive
  Hanover, MD 21076–1320

NASA/TM—2003-212692

Correlation of Radiation Dosage With Mechanical Properties of Thin Films

R.L. Newton
Marshall Space Flight Center, Marshall Space Flight Center, Alabama

National Aeronautics and
Space Administration

Marshall Space Flight Center • MSFC, Alabama 35812

August 2003

Acknowledgments

The author gratefully acknowledges the support of Charles Griffith of NASA Marshall Space Flight Center (MSFC) and Tom Geer of Oak Ridge National Laboratory (ORNL) for assistance with sample polishing. Also, the work of Jimmy Coston, MSFC, on the scanning electron microscopy analysis is greatly appreciated. Many thanks to Gene Ice, ORNL, for his assistance with x-ray diffraction analysis and Michael Lance of the HTML Facility at ORNL for assistance with the Raman experiments.

TRADEMARKS

Trade names and trademarks are used in this report for identification only. This usage does not constitute an official endorsement, either expressed or implied, by the National Aeronautic and Space Administration.

Available from:

NASA Center for AeroSpace Information
7121 Standard Drive
Hanover, MD 21076–1320
(301) 621–0390

National Technical Information Service
5285 Port Royal Road
Springfield, VA 22161
(703) 487–4650

TABLE OF CONTENTS

1. PURPOSE 1

2. BACKGROUND 2

   2.1 Crystal Structure of Diamond and Graphite 2
   2.2 Other Factors Influencing Thin Film Mechanical Properties 3
   2.3 Ion Implantation and Modeling Software 3
   2.4 Implant-Related Defects—Overview 4
   2.5 Implant-Related Defects—Vacancies 4
   2.6 Implant-Related Defects—Interstitials 4
   2.7 Implant-Related Defects—Hydrogen and Protons 5
   2.8 Raman Spectroscopy 6
   2.9 Micro-X-Ray Diffraction 7
   2.10 Preliminary Experiments and Related Publications 8

3. EXPERIMENTAL PROCEDURE 9

   3.1 Proton Implantation 9
   3.2 Specimen Preparation and Scanning Electron Microscopy 11
   3.3 Micro-Raman Spectroscopy 11
   3.4 Micro-X-Ray Diffraction 12

4. EXPERIMENTAL RESULTS 13

   4.1 Visual Examination 15
   4.2 Scanning Electron Microscopy—Diamond Top Surface 15
   4.3 Micro-Raman Analysis—Diamond Top Surface 18
   4.4 Scanning Electron Microscopy Analysis—Diamond Cross Section 20
   4.5 Micro-Raman Analysis—Diamond Cross Section 23
   4.6 Scanning Electron Microscopy Analysis—Silicon Top Surface 30
   4.7 Micro-Raman Analysis—Silicon Top Surface 33
   4.8 Scanning Electron Microscopy Analysis—Silicon Cross Section 35
   4.9 Micro-Raman Analysis—Silicon Cross Section 37
   4.10 Micro-X-Ray Diffraction 39

TABLE OF CONTENTS (Continued)

5. DISCUSSION 41

5.1 Implantation Modeling—Diamond 41
5.2 Hydrostatic Strain Calculations via Raman Spectroscopy—Diamond 42
5.3 Deviatoric Strain Calculations via Micro-X-Ray Diffraction—Diamond 44
5.4 Additional Strain Analysis 45
5.5 Phase Transition Thresholds—Diamond 46
5.6 Implantation Modeling and Raman Experimental Results—Silicon 46

6. CONCLUSIONS AND FUTURE WORK 49

REFERENCES 52

LIST OF FIGURES

1. The three-dimensional crystal structure in an 8- by 8-unit cell of: (a) Diamond, where each carbon atom is surrounded by its four nearest neighbors and connected by covalent bonds, and (b) graphite, which has high in-plane strength but weak bonding between planes 2

2. The calculated production, using the TRIM code, of vacancies in diamond caused by 600 keV protons. Due to the size of the protons and the small cross section of the diamond, the ions travel in an essentially straight path, causing little lattice damage until reaching the end of their trajectory. Silicon is shown for comparison 5

3. Representative Raman spectra of diamond, graphite, glassy carbon, and amorphous carbon 6

4. Schematic sample and instrumental geometry for a micro-XRD experiment 7

5. Schematic cross section of polycrystalline diamond thin film prepared by MPACVD. The diamond is grown directly on the silicon substrate. Growth time for the film was 20 hr 9

6. Schematic cross section of the polycrystalline silicon thin film prepared by LPCVD. Good film adhesion to the substrate is ensured by first depositing a thin film of silicon dioxide 9

7a. Wide-angle view of the accelerator facility. The sample port is located near the far right in this photograph 10

7b. Closeup of sample port used during implantation. Peltier cooling units are located below the cooling fin. Also, a fan is located near the left side of the port to aid in cooling 10

8a. Closeup of backside of sample holder. The white squares are individual Peltier cooling units 10

8b. Schematic of the sample orientation during implantation. This same edge-on configuration was maintained throughout the experimental investigation 10

9. Diamond specimen mounted in quick-setting epoxy. The sample is mounted edge-on for analysis 11

LIST OF FIGURES (Continued)

10. Experimental setup of the micro-Raman system used in data collection 11

11a. Overview of the Synchrotron Radiation Facility at Argonne National Laboratory located near Chicago, IL 12

11b. Experimental setup of a sample on the table inside the end station in 34ID–E 12

12. End plate of the accelerator beam line where specimens were placed during implantation procedures. This "after" photograph shows the most heavily irradiated specimens, the 2×10^{17} H^+/cm^2 silicon square (upper left section of center circle) and diamond (center circle) and diamond specimens 13

13a. Log-log plot of proton flux plotted as a function of proton dosage 14

13b. Total flux and temperature plotted against total time for the 2×10^{15} H^+/cm^2 implant using the current integrator to monitor dosage 14

13c. Total flux and temperature plotted against total time for the 2×10^{16} H^+/cm^2 14

13d. Total flux and temperature plotted against total time for the 2×10^{17} H^+/cm^2 implant using the current integrator to monitor dosage. Although this implant took days, both the specimen temperature and accelerator output were maintained at a constant level 14

14. Photograph showing all specimens used in this investigation. The silicon samples are taped to the surface of the diamond to ensure equal implantation dosages. The black lines on two of the samples were used to outline the beam diameter 15

15. SEM of the top surface of the as-deposited polycrystalline diamond film: (a) Wide-angle and (b) closeup 16

16. SEM of the top surface of the 2×10^{15} H^+/cm^2-proton-implanted polycrystalline diamond film: (a) Wide-angle and (b) closeup 16

17. SEM of the top surface of the 2×10^{16} H^+/cm^2-proton-implanted polycrystalline diamond film: (a) Wide-angle and (b) closeup 17

18. SEM of the top surface of the 2×10^{17} H^+/cm^2-proton-implanted polycrystalline diamond film: (a) Wide-angle and (b) closeup 17

LIST OF FIGURES (Continued)

19. Negative images of SEM micrographs of: (a) The as-deposited and (b) the heavily irradiated diamond material 18

20. Micro-Raman spectra of the top surface of: (a) The as-deposited polycrystalline diamond wafer with an inset that shows Lorentzian fit to experimental data, and (b) the 2×10^{15} H^+/cm^2-implanted polycrystalline diamond wafer 18

21. Micro-Raman spectra of the top surface of: (a) The 2×10^{16} H^+/cm^2-implanted polycrystalline diamond wafer with an inset that shows implantation-induced damage, and (b) the 2×10^{17} H^+/cm^2-implanted polycrystalline diamond wafer with an inset that shows implantation-induced damage 19

22. Graph showing first-order diamond peak position and first-order diamond peak FWHM as a function of proton dosage 20

23. SEM micrograph showing the edge surface of: (a) The as-deposited polycrystalline diamond wafer with the diamond film/silicon substrate interface indicated by the white horizontal line near the lower portion of the figure, and (b) the 2×10^{15} H^+/cm^2-implanted polycrystalline diamond wafer 21

24a. SEM micrograph showing the edge surface of the 2×10^{16} H^+/cm^2-implanted polycrystalline diamond wafer 21

24b. Wide-angle SEM micrograph showing the edge surface of the 2×10^{17} H^+/cm^2-implanted polycrystalline diamond wafer. The film/substrate interface is seen in the lower half of the figure 21

25. Closeup SEM micrograph showing the edge surface of the 2×10^{17} H^+/cm^2-implanted polycrystalline diamond wafer 22

26. Negative images of SEM micrographs of: (a) The as-deposited polycrystalline diamond film and (b) the 2×10^{17} H^+/cm^2-implanted polycrystalline diamond film 23

27. Schematic illustrating the direction of proton implantation and specimen orientation for the micro-Raman cross-sectional analysis 23

28. Micro-Raman spectra as a function of depth across the surface of: (a) The as-deposited polycrystalline diamond film and (b) the 2×10^{15} H^+/cm^2 polycrystalline diamond film 24

LIST OF FIGURES (Continued)

29. Micro-Raman spectra as a function of depth across the surface of the 2×10^{16} H^+/cm^2 polycrystalline diamond film 25

30. Analysis of the first-order diamond peak position and first-order diamond FWHM as a function of cross-sectional depth in the 2×10^{16} H^+/cm^2-irradiated polycrystalline diamond film 26

31. Micro-Raman spectra as a function of depth across the surface of the 2×10^{17} H^+/cm^2 polycrystalline diamond film 27

32. Representative spectra detailing the curve fitting used to examine the damaged region in the 2×10^{17} H^+/cm^2-implanted diamond film 27

33a. Analysis of the first-order diamond peak position and first-order diamond FWHM as a function of cross-sectional depth in the 2×10^{17} H^+/cm^2-irradiated polycrystalline diamond film 28

33b. Comparison of the first-order diamond peak position as a function of first-order diamond peak FWHM at ≈4 μm in depth, near the EOR for the proton implantation 28

34. Summary chart for the entire implantation series showing the variation in: (a) The first-order peak position as a function of depth and (b) the first-order FWHM as a function of depth 29

35. SEM micrograph of the top surface of the as-deposited polycrystalline silicon wafer: (a) Wide-angle and (b) closeup 30

36. SEM micrograph of the top surface of the 2×10^{15} H^+/cm^2-implanted polycrystalline silicon wafer: (a) Wide-angle and (b) closeup 31

37. SEM micrograph of the top surface of the 2×10^{16} H^+/cm^2-implanted polycrystalline silicon wafer: (a) Wide-angle and (b) closeup 31

38. SEM micrograph of the top surface of the 2×10^{17} H^+/cm^2-implanted polycrystalline silicon wafer: (a) Wide-angle and (b) closeup 32

39. Negative images of the wide-angle SEM micrographs of: (a) The as-deposited and (b) 2×10^{17} H^+/cm^2-implanted polycrystalline silicon films 32

40. Typical Raman signatures from crystalline silicon (top), polycrystalline silicon (middle), and amorphous silicon (bottom) 33

LIST OF FIGURES (Continued)

41. Micro-Raman spectra of the top surface of: (a) The as-deposited polycrystalline silicon wafer and (b) the 2×10^{15} H^+/cm^2-implanted polycrystalline silicon wafer 34

42. Micro-Raman spectra of the top surface of: (a) The 2×10^{16} H^+/cm^2-implanted polycrystalline silicon wafer and (b) the 2×10^{17} H^+/cm^2-implanted polycrystalline silicon wafer 34

43. Polycrystalline silicon peak position and FWHM as a function of proton dosage for the entire silicon series 35

44. SEM micrograph of the edge of: (a) The as-deposited polycrystalline silicon, with the interface between the polycrystalline silicon and single-crystal silicon evident in the lower portion of the micrograph and (b) the 2×10^{15} H^+/cm^2-implanted polycrystalline silicon sample with no noticeable effects of the implant. The interface between film and substrate is noticeable in the lower portion of the figure 36

45. SEM micrograph of the edge of the 2×10^{16} H^+/cm^2-implanted polycrystalline specimen. No visible effects from the implantation are evident 36

46. SEM micrograph of the 2×10^{17} H^+/cm^2-implanted polycrystalline silicon: (a) Wide-angle—the polycrystalline silicon layer indicates an interface not seen in the other specimens and (b) closeup (outlined area, shown in greater detail)—an interface ≈8 μm from the top surface is clearly visible 37

47. Micro-Raman spectra as a function of depth across: (a) The cleaved surface of the as-deposited polycrystalline silicon film and (b) the 2×10^{15} H^+/cm^2-implanted polycrystalline silicon film 38

48. Micro-Raman spectra as a function of depth across the cleaved surface of: (a) The 2×10^{16} H^+/cm^2-implanted polycrystalline silicon film and (b) the 2×10^{17} H^+/cm^2-implanted polycrystalline silicon film 38

49. Summary chart for the entire polycrystalline silicon implantation series showing the variation in: (a) Peak position as a function of depth and (b) FWHM as a function of depth 39

50. Components as a function of depth for the deviatoric strain tensor for the 2×10^{17} H^+/cm^2-implanted diamond specimen for: (a) Normal components and (b) shear components 40

LIST OF FIGURES (Continued)

51. Comparison of depth-dependent Raman analysis as a function of depth for helium ion implantation into single-crystal diamond (solid dots and dotted line) as opposed to proton implantation into polycrystalline diamond (hollow dots and dashed line) 42

52. First-order diamond peak of 2×10^{17} H^+/cm^2-implanted diamond. While the peak is broad, skewed, and shifted downward, peak splitting is not observed 43

53. Calculated elastic strain as a function of depth for: (a) The 2×10^{16} H^+/cm^2-implanted diamond specimen—the elastic strain limit for certain diamond-based MEMS devices is exceeded in the first 8 μm of the film, and (b) the 2×10^{17} H^+/cm^2-implanted diamond specimen—elastic strain limit for certain diamond-based MEMS devices is exceeded in the first 10 μm of the film 43

54. In the polycrystalline state, the crystallites are randomly oriented in three dimensions 44

55. Diamond values for: (a) Tension and shear and (b) stress and strain. The critical value of strain for the transition from diamond to graphite is greatly diminished in the tension configuration 45

LIST OF TABLES

1. Representative mechanical properties of diamond, graphite, and silicon 3

2. Summary of calculated implantation range and straggles of 600 keV protons using TRIM 5

3. Implantation parameters for proton implantation experiment 10

LIST OF ACRONYMS

BC	bond centered
BCA	binary collision approximation
C-C	carbon-carbon
CCD	charged-coupled device
CVD	chemical vapor deposition
EOR	end of range
FWHM	full width at half maximum
LPCVD	low pressure chemical vapor deposition
MEMS	microelectromechanical systems
MPACVD	microwave plasma-assisted chemical vapor deposition
MSFC	Marshall Space Flight Center
ORNL	Oak Ridge National Laboratory
SEM	scanning electron microscopy
SRIM	Stopping and Range of Ions in Matter (program)
TRIM	Transport of Ions in Matter (program)
XRD	x-ray diffraction

NOMENCLATURE

D_c	critical dose
$d\sigma$	collision cross section
E	elastic modulus
E_d	displaced energy
GPa	gigapascal
H	hardness
h	Miller indice
I	intensity
k	Miller indice
n	diffraction order
Rp	range (μm)
v_o	frequency of initial Raman signal
v_s	frequency of shifted Raman signal
Δ	strain components
ΔRp	straggle (μm)
ε	strain
ρ	density
σ	stress

TECHNICAL MEMORANDUM

CORRELATION OF RADIATION DOSAGE WITH MECHANICAL PROPERTIES OF THIN FILMS

1. PURPOSE

The objective of this investigation was to examine the relationship between irradiation level (proton dose), microstructure, and stress levels in chemical vapor deposited (CVD) diamond and polysilicon films using cross-sectioned specimens. However, the emphasis was placed on the diamond specimens because diamond holds much promise for use in advanced technologies. The use of protons allows not only the study of the charged particle that may cause the most microstructural damage in Earth-orbit microelectromechanical systems (MEMS) devices, but also allows the study of relatively deeply buried damage inside the diamond material. Using protons allows these studies without having to resort to megaelectronvolt implant energies that may create extensive damage due to the high energy that is needed for the implantation process. Since MEMS devices operating in space will not have an opportunity to reverse radiation damage via annealing, only nonannealed specimens were investigated. The following three high spatial resolution techniques were used to examine these relationships: (1) Scanning electron microscopy (SEM), (2) micro-Raman spectroscopy, and (3) micro-x-ray diffraction (XRD).

2. BACKGROUND

A brief review of the relevant microstructures, radiation effects, and experimental techniques used in this project are presented in this section. Similarities of and differences between diamond and graphite carbon-carbon (C-C) bonds are demonstrated.

2.1 Crystal Structure of Diamond and Graphite

Diamond belongs to the crystallographic space group Fd3m (No. 227) with site 8a (site symmetry 43m) filled. Not surprisingly, the structure is commonly referred to as the diamond structure. In this structure, atoms also occupy the tetrahedral interstitial sites. Each atom is covalently bonded to four adjacent carbon atoms via sp^3 bonding, with each bond making an angle of 109° 28′ with four other carbon atoms. Much of the hardness of diamond is a result of this strong, tetrahedral bonding. Figure 1 illustrates an 8- by 8-unit cell of diamond and graphite.

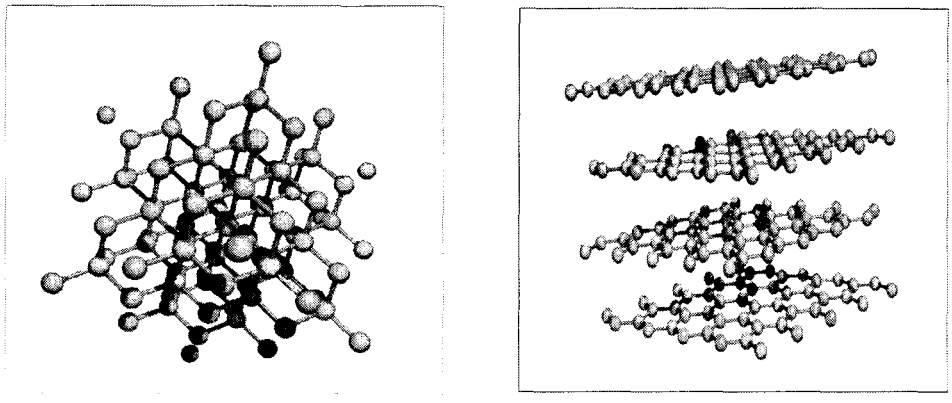

(a) (b)

Figure 1. The three-dimensional crystal structure in an 8- by 8-unit cell of: (a) Diamond, where each carbon atom is surrounded by its four nearest neighbors and connected by covalent bonds, and (b) graphite, which has high in-plane strength but weak bonding between planes.

Graphite belongs to the crystallographic space group $P6_3mmc$ with a=2.46 Å and c=6.69 Å. It has a structure containing layers of atoms that are arranged at the corners of contiguous hexagons. The ease with which layers slide against each other is consistent with the much larger distance between carbon atoms in different layers than between carbon atoms in the same layer. The carbon atoms are bonded via sp^2 orbitals.

2.2 Other Factors Influencing Thin Film Mechanical Properties

Not only do atomistic—or lattice—effects, such as those examined in section 2.1, influence material performance, but other factors, such as deposition, grain growth, grain size, and annealing, contribute to the mechanical performance of CVD diamond thin films.[1–3] Table 1 presents an overview of some experimentally measured mechanical properties of CVD diamond, graphite, and silicon for comparison.

Table 1. Representative mechanical properties of diamond, graphite, and silicon.[4–7]

Material	Density, ρ (Kg/m^3)	Modulus, E (GPa)	Hardness, H (GPa)
Diamond	3,510	1,035	117
Graphite	2,260	≈800	2.35
Silicon	2,330	129–187	11

The internal, or residual, stress in CVD diamond films plays one of the more important roles in determining mechanical performance.[8–10] This stress may be either intrinsic or thermal. Intrinsic stress, also known as growth stress, develops during film nucleation. Internal stress and intrinsic stress are the cumulative results of the chemical and microstructural defects created during deposition. Thermal stress is due to the different thermal expansion of the coating and substrate and occurs during cooldown from the deposition temperature. These stresses may be either compressive or tensile. Compressive stress during deposition may lead to buckling and blistering of the film, and tensile stress may lead to cracking.

2.3 Ion Implantation and Modeling Software

Much of our understanding of how radiation affects materials, such as diamond, comes from ion-implantation studies. Ion implantation is a method that forces high kinetic energy ions into solid materials. This technique is used extensively in the field of microelectronics as a means of introducing dopant atoms into semiconductors. The transfer of energy between ion and solid is divided into two processes: (1) Nuclear (elastic) collisions and (2) electronic (inelastic) collisions. The large density of electrons and the high frequency of ion-electron collisions account for much of the slowing down of ions in materials, yet this process seldom displaces host atoms. It is the nuclear collisions of energetic ions and lattice atoms that displace the host atoms from their equilibrium position and cause the bulk of the structural damage.

Ion implantation software has been around for decades. The goal of the software is to be able to predict the final ion distribution in the target. Most conventional methods used to calculate ion ranges are based on binary collision approximation (BCA).[11] These methods treat the movement of ions in the sample as a succession of individual collisions between the recoil atoms and the sample's host atoms.

For each individual collision, the classical scattering integral is solved by numerical integration. By far, the most widely used BCA program is the Transport of Ions in Matter (TRIM); its most recent version is called the Stopping and Range of Ions in Matter (SRIM).[6] SRIM was used exclusively for all theoretical ion-substrate calculations in this project.

2.4 Implant-Related Defects—Overview

While uncertainty remains concerning the mechanism that causes gross microstructural changes in ion-implanted diamond, the defects created are thought to be primarily composed of vacancies and interstitials. Classical molecular dynamics and classical Monte Carlo calculations have been used to investigate the energetics involved in the formation of vacancies and interstitials in diamond and the relaxation of the crystal around these defects.[12] One of the key findings was that the relaxation of the carbon atoms around the vacancy left behind by the displaced atom is always outward with an average displacement of 0.23 Å. Noting the fact that the C-C length in diamond is 1.54 Å and the C-C length in graphite is 1.46 Å, the tendency to shorten the bonds makes them more graphitic in nature. It was also found that a third C-C of 1.51 Å is also present in the defect region. This transitional material between diamond and graphite has been observed experimentally.

The above theoretical calculations simulate the final stage of the stopping process of a carbon atom that is being displaced in diamond via ion implantation or some other radiation process. These damaged regions will contain a mixture of sp^3- and sp^2-bonded carbon. Substrate temperature at the time of implantation has also been shown to have a significant impact on the resulting damage as well as beam flux.[13] However, unlike most other implanted species, proton implantation appears to create not only vacancies and interstitials but an additional carbon-hydrogen defect structure as well.

2.5 Implant-Related Defects—Vacancies

Vacancies in diamond have been extensively studied and can have a strong impact on the electrical and optical properties of diamond-based devices. Since silicon and diamond possess the same crystalline structure, silicon vacancy study has aided in diamond vacancy understanding. Vacancies are known to be mobile above 600 °C and can exist in neutral, negative, and positive charge states.[14] Calculations indicate that the four atoms surrounding the vacancy relax outward by a few tenths of an angstrom.[15] Vacancy diffusion near the surface has a lower diffusion barrier than vacancy diffusion in the bulk.[16] Divacancies, the removal of two neighboring atoms from the diamond structure, have also received theoretical and experimental attention.[17] Vacancies are thought to be responsible for the 1,490 cm^{-1} peak observed in Raman spectroscopy of irradiated diamond material.

2.6 Implant-Related Defects—Interstitials

Unlike the diamond vacancy, the diamond self-interstitial—one of the few self-interstitials to be detected experimentally in any semiconductor—has only recently been identified.[18] With respect to self-interstitial defects, the four possible defects are (1) tetrahedral, (2) hexagonal, (3) bond-centered (BC), and (4) the <100> and <110> split interstitials. While the diamond vacancy is mobile only at elevated temperatures, the diamond interstitial is mobile at much lower temperatures. The 1,630 cm^{-1} Raman peak is associated with this defect.

2.7 Implant-Related Defects—Hydrogen and Protons

When a proton hits the nucleus of a carbon atom with sufficient energy, it knocks the carbon atom off its lattice site, and that displaced atom may collide with other atoms via a cascade effect. Although diamond has the highest known atomic density (1.764×10^{23} atoms/cm^3), the size of its nuclear radius results in a small cross section for interaction with incident protons. Since protons are charged, the end result is that protons are primarily slowed by electronic means, and nuclear effects are only significant near the terminal end of the ions path. This is illustrated in figure 2 for diamond and silicon by observing that ions penetrating the surface create few vacancies and undergo little deflection as they pass through the materials.

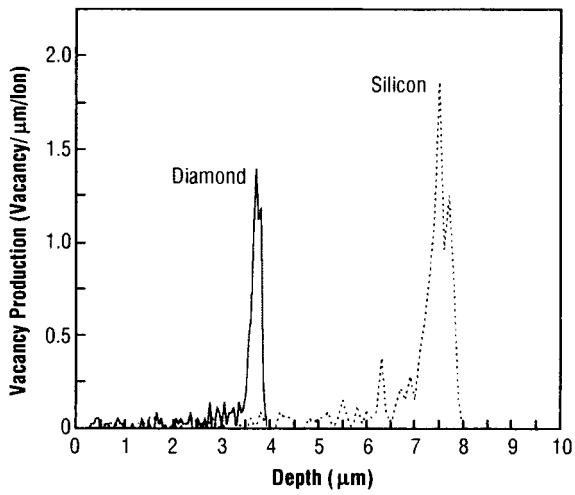

Figure 2. The calculated production, using the TRIM code, of vacancies in diamond caused by 600 keV protons. Due to the size of the protons and the small cross section of the diamond, the ions travel in an essentially straight path, causing little lattice damage until reaching the end of their trajectory. Silicon is shown for comparison.

For comparison, silicon—atomic density of 5×10^{22} atoms/cm^3 (28 percent of the atomic density of diamond)—has a much broader final distribution of protons as compared to diamond. This is because of the increased reaction cross section, which is due to the larger nucleus of the silicon atom. However, in both diamond and silicon, over 99 percent of the incident energy loss is due to electronic interactions. The parameters used and results of TRIM calculations are summarized in table 2 for a simulation of protons deposited into a 4-µm-thick diamond film and a 10-µm-thick silicon film.

Table 2. Summary of calculated implantation range and straggles of 600 keV protons using TRIM.

Specimen	Range, R_p (µm)	Straggle, ΔR_p (µm)	Displacement Energy, E_d (eV)	Vacancies per Ion	Energy Loss to Ionization (%)
Diamond	3.70	0.0798	25	6.0	99.80
Silicon	7.51	0.333	15	30.9	99.78

Hydrogen implantation in diamond produces much less structural damage than implantation with larger ions. However, unlike other implant species, evidence to date suggests that in addition to creating vacancies and interstitials, hydrogen implantation appears to create an immobile hydrogen aggregate or lattice defect.[19] Goss et al. have performed ab initio analysis and have proposed that hydrogen occupies a BC position within the diamond.[20] Experimentally, Machi et al. used microscanning heavy ion-elastic recoil detection analysis and observed that implanted hydrogen in diamond self-traps in the BC and/or the hydrogen position center where it remains tightly bonded, even up to temperatures of 1,473 K.[21,22]

2.8 Raman Spectroscopy

Carbon-based materials, specifically diamond, have been studied extensively by Raman microscopy.[23] Raman analysis is fast and nondestructive. Figure 3 shows the first-order Raman line of sp^3 carbon (diamond), located at $\approx$1,332 cm^{-1}; a broad band, located at $\approx$1,550 cm^{-1}, which is characteristic of sp^2-bonded carbon (graphite); glassy carbon, composed of two large, broad peaks; and amorphous carbon, presenting a large asymmetric peak at $\approx$1,500 cm^{-1}.

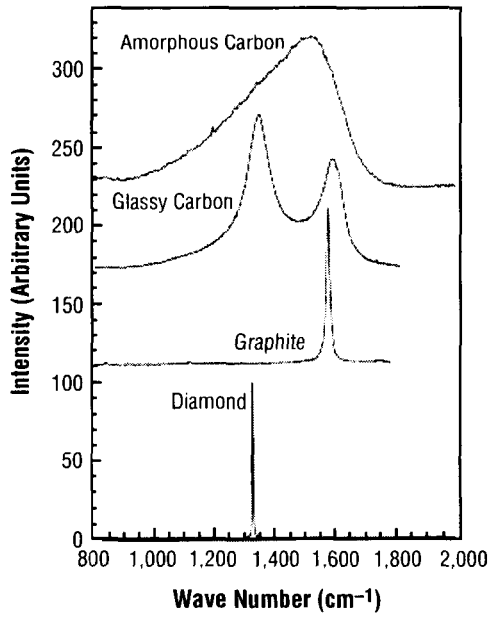

Figure 3. Representative Raman spectra of diamond, graphite, glassy carbon, and amorphous carbon.[24]

Peak broadening is attributed to lifetime broadening on the phonon. This implies structural disorder. Peak position; i.e., shift, depends primarily on the C-C distance. A deformation that causes this distance to increase results in a C-C vibration frequency decrease.

To obtain a Raman measurement, an incident laser beam is used to illuminate the specimen surface. Raleigh-scattered light is rejected by passing the scattered light through a double monochrometer, Raman-shifted wavelengths are detected via a photodetector, and for micro-Raman

measurements, a microscope is used to focus the laser on the surface of the specimen. With suitable objectives, spot sizes on the order of a few microns in diameter are achievable. The beam diameter of the Raman laser used for measurements in this investigation was ≈1 μm.

2.9 Micro-X-Ray Diffraction

XRD has been an extremely useful analytical tool for examining the microstructure of materials for many decades. It is relatively straightforward, quick, and nondestructive. Additionally, in many cases, no sample preparation is needed. There have been many XRD studies examining CVD diamond and several that have examined CVD diamond using both micro-Raman and XRD studies.[25–27] However, only in the past few years have the experimental tools been available to allow the XRD study of materials with submicron spatial resolution. This has been accomplished by the development of ultrabrilliant third-generation synchrotron x-ray sources with advanced x-ray optics.[28]

Using differential-aperture x-ray microscopy, the technique used in this investigation, microstructure and stress and strain measurements are made with submicron spatial resolution in three dimensions. By using charge-coupled device (CCD) area detection, polychromatic x-ray microbeams, and computer reconstruction, Laue diffraction patterns are extracted as a function of depth along the penetration direction of the microbeam.[29]

Figure 4 is a schematic of the experimental setup needed to perform micro-XRD analysis. When strain distributions within a material are needed, a large number of measurements are needed. A broad-band-pass microbeam intercepts the sample and illuminates a small number of crystal grains. The overlapping Laue patterns from the grains are recorded on an area detector and fit to find the center of each reflection. The pattern is then indexed to determine the indices of each reflection and the number of reflecting grains. The texture and orientation and strain tensors are then determined for the illuminated grains. Strain measurements of less than 10^{-4} are possible using this technique. For a detailed example of this procedure, see Larson et al.[29]

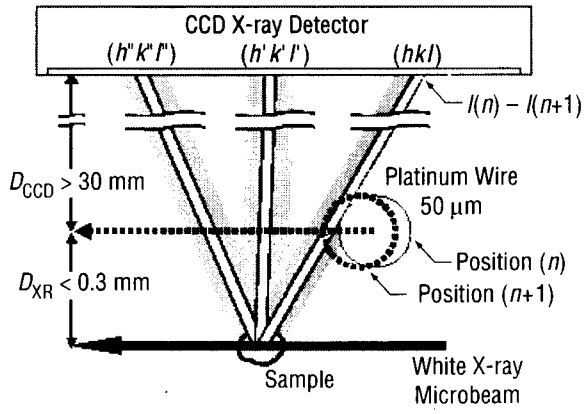

Figure 4. Schematic sample and instrumental geometry for a micro-XRD experiment.[29]

2.10 Preliminary Experiments and Related Publications

A preliminary experimental investigation was undertaken prior to the present study. This was done in order to ascertain whether or not thin films of diamond could be satisfactorily cut and mounted in the cross-sectional configuration. The experiment consisted of proton and electron implantation into CVD diamond thin films followed by micro-Raman and nanoindention analysis. The results were presented during the ASTM International Fall Meeting in Orlando, FL, November, 2000. The results did indicate that mounting thin diamond films for cross-sectional analysis was challenging but that further experimentation was warranted. Selected results of the micro-Raman analysis of the proton-implanted diamond were presented at the Fifth Conference on Aerospace Materials, Processes, and Environmental Technology in Huntsville, AL, September 16–18, 2002.

3. EXPERIMENTAL PROCEDURE

Polycrystalline diamond, ≈20 μm in thickness, was prepared at Vanderbilt University on a 5.08-cm (2-in) single-crystal silicon substrate by using microwave plasma-assisted CVD (MPACVD) at a temperature of 800 °C and a pressure of 110 torr. The hydrogen flow rate was 479 sccm, and the methane flow rate was 18 sccm with a microwave power of 5 kW. The total time of film deposition was 20 hr. The schematic presented in figure 5 illustrates a cross-sectional view of the as-deposited wafer.

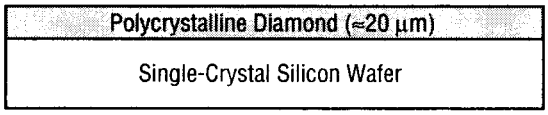

Figure 5. Schematic cross section of polycrystalline diamond thin film prepared by MPACVD. The diamond is grown directly on the silicon substrate. Growth time for the film was 20 hr.

Polycrystalline silicon was procured from Cermat Technologies, Murray Hill, NJ. An approximately 22-μm film of polycrystalline silicon was deposited on top of 1,000 Å of silicon dioxide, which was grown on a single-crystal silicon wafer. The polycrystalline silicon was deposited by low-pressure CVD at a temperature of 615 °C and a pressure of 400 mtorr using dilute silane in nitrogen as a precursor. A cross-sectional schematic of this wafer is shown in figure 6.

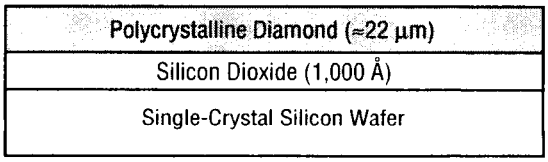

Figure 6. Schematic cross section of the polycrystalline silicon thin film prepared by LPCVD. Good film adhesion to the substrate is ensured by first depositing a thin film of silicon dioxide.

3.1 Proton Implantation

The samples were implanted with protons using an NEC Model 5SDH–2 Pelletron® accelerator (fig. 7a) located at Alabama A&M University in Huntsville, AL. Figure 7b shows a closeup of the specimen mounting area, figure 8a shows a view of the peltier cooling units placed on the back plate for cooling purposes, and figure 8b shows the edge-on configuration that will be used throughout the investigation. Table 3 gives the implantation parameters. By using a low current density and supplemental cooling hardware, sample heating was keep to a minimum.

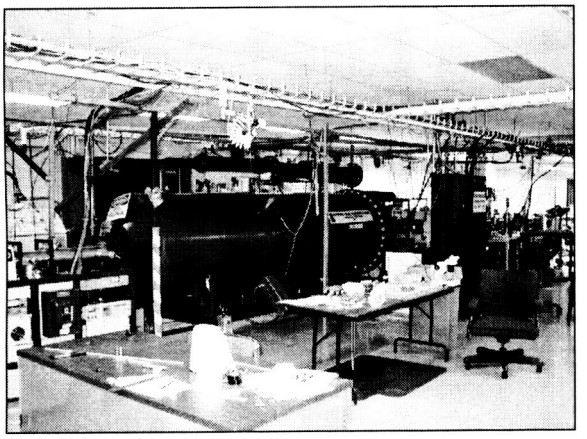

Figure 7a. Wide-angle view of the accelerator facility. The sample port is located near the far right in this photograph.

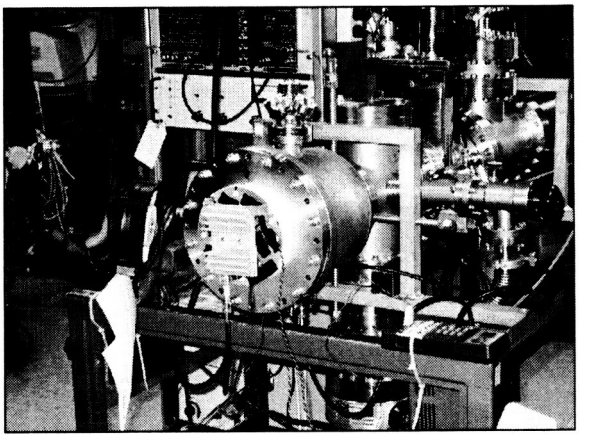

Figure 7b. Closeup of sample port used during implantation. Peltier cooling units are located below the cooling fin. Also, a fan is located near the left side of the port to aid in cooling.

Figure 8a. Closeup of backside of sample holder. The white squares are individual Peltier cooling units.

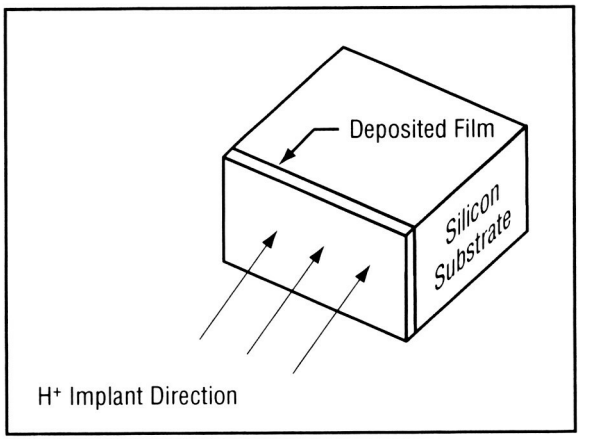

Figure 8b. Schematic of the sample orientation during implantation. This same edge-on configuration was maintained throughout the experimental investigation.

Table 3. Implantation parameters for proton implantation experiment.

Element	Implantation Dose (Ions/cm^2)	Implantation Energy (keV)	Current Density (uA/cm^2)	Vacuum (torr)
H^+	2×10^{15}	600	2	$1.2\text{–}6\times10^{-7}$
H^+	2×10^{16}	600	2	$1.2\text{–}6\times10^{-7}$
H^+	2×10^{17}	600	2	$1.2\text{–}6\times10^{-7}$

3.2 Specimen Preparation and Scanning Electron Microscopy

SEM micrographs of the specimens were taken using an ElectroScan Environmental SEM located at Marshall Space Flight Center (MSFC) in Huntsville, AL. After irradiation, the samples were cut and mounted on edge. They were then polished by personnel at both MSFC and by personnel at the Oak Ridge National Laboratory (ORNL) in Oak Ridge, TN. Figure 9 shows a cut, mounted, and polished diamond specimen.

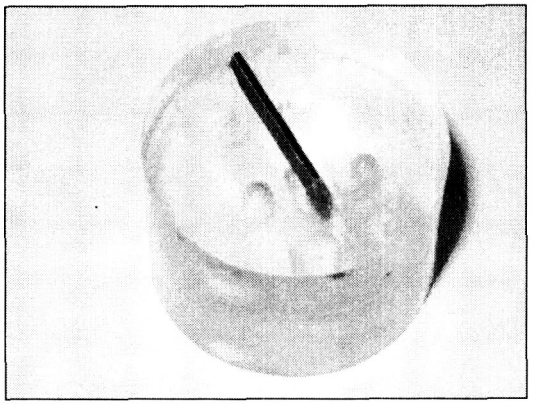

Figure 9. Diamond specimen mounted in quick-setting epoxy. The sample is mounted edge-on for analysis.

3.3 Micro-Raman Spectroscopy

Raman spectra were collected at ORNL with a JY® Dilor XY800 Raman microprobe that was configured as a single-stage spectrograph using the microscope with ≈1 μm resolution. A Coherent® Innova® 308C Ar^+ ion laser, 514.5 nm and 100 mW output power, was used to excite the sample. This equipment is shown in figure 10.

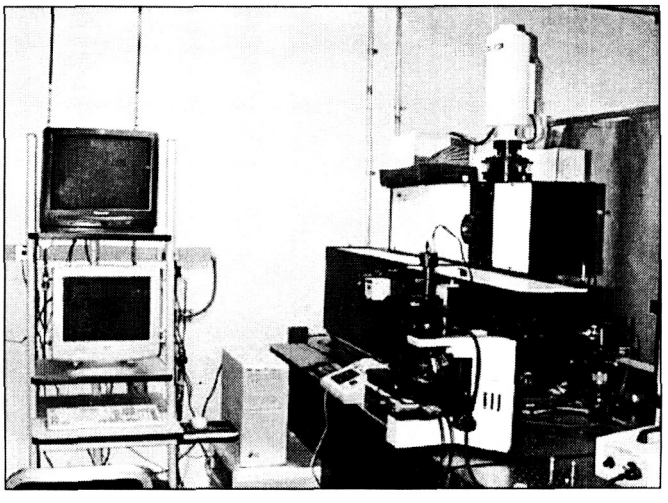

Figure 10. Experimental setup of the micro-Raman system used in data collection.

3.4 Micro-X-Ray Diffraction

The micro-XRD measurements were performed at the 34ID–E facility, Advanced Photon Source, Argonne National Laboratories (fig. 11a). The 34ID–E facility is located in one of the lab/office modules that surround the ring. The sample setup in the lab module is shown in figure 11b. The experimental conditions were as follows:

- Microbeam size:

  – Horizontal—0.4 μm.
  – Vertical—0.5 μm.

- Undulator: 12-keV, 4-μm taper, and –50 microrad steering.

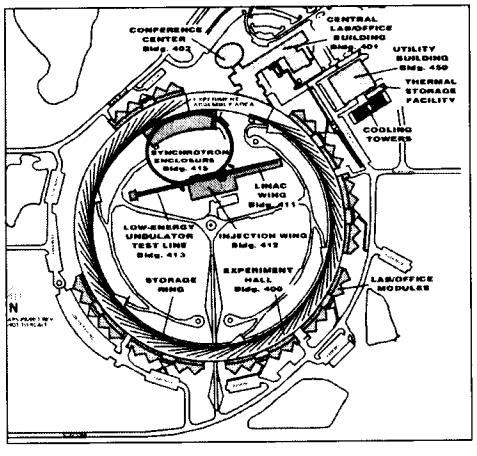

Figure 11a. Overview of the Synchrotron Radiation Facility at Argonne National Laboratory located near Chicago, IL.

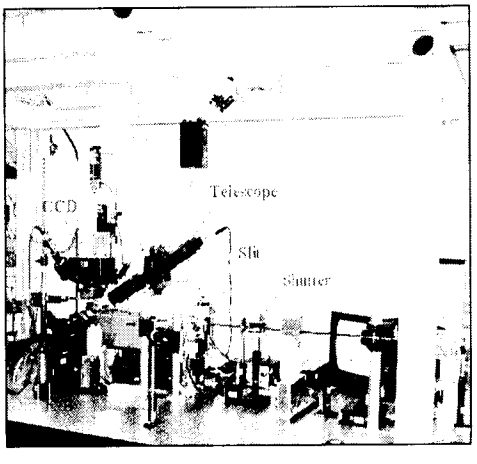

Figure 11b. Experimental setup of a sample on the table inside the end station in 34ID–E.

4. EXPERIMENTAL RESULTS

In this section, the details of the visual inspection, the top-surface and cross-sectional SEM and micro-Raman analyses for diamond and silicon, and the micro-XRD results will be presented and discussed. The diamond specimens were taken from one 5.08-cm (2-in) wafer. The silicon specimens were obtained from one 12.7-cm (5-in) wafer. To ensure an equal proton dose implant for both the diamond and silicon specimens, the implantations were performed simultaneously at each fluence level. This was accomplished by piggybacking the silicon sample to the top surface of the diamond specimen using double-sided tape. Figure 12 shows the 2×10^{17} H^+/cm^2-implanted specimen mounted on the target plate after the completion of the irradiation.

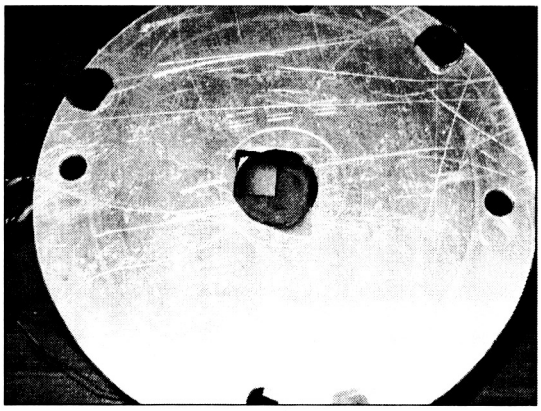

Figure 12. End plate of the accelerator beam line where specimens were placed during implantation procedures. This "after" photograph shows the most heavily irradiated specimens, the 2×10^{17} H^+/cm^2 silicon (square in upper left section of center circle) and diamond (center circle) specimens.

The irradiation rate was kept below 10^{13} $H^+/cm^2/s$ so that nonlinear effects could be avoided. The flux (protons/cm^2 s) versus fluence (protons/cm^2) is presented in figure 13a. The output of the accelerator was constant throughout the duration of the each implantation profile, shown graphically in figures 13b–13d. The current integrator recordings indicated a linear behavior. The temperature, as measured at a thermocouple attached to the end plate of the irradiation chamber, remained constant throughout the implantation regimes.

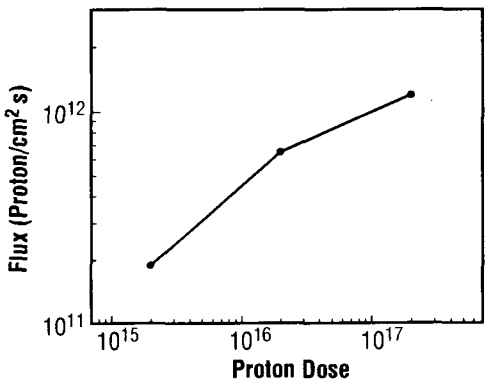

Figure 13a. Log-log plot of proton flux plotted as a function of proton dosage.

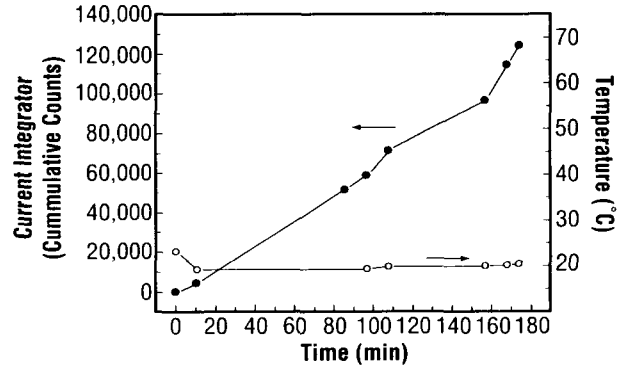

Figure 13b. Total flux and temperature plotted against total time for the 2×10^{15} H^+/cm^2 implant using the current integrator to monitor dosage.

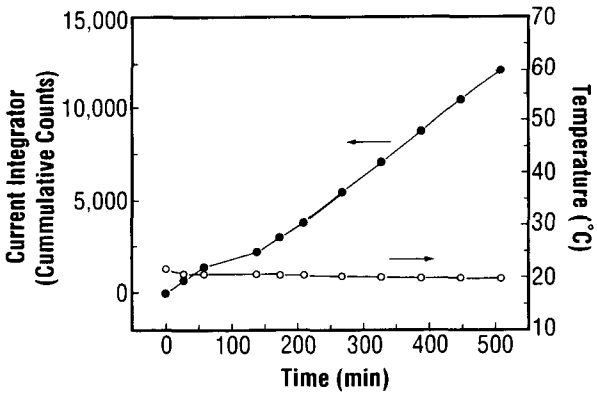

Figure 13c. Total flux and temperature plotted against total time for the 2×10^{16} H^+/cm^2.

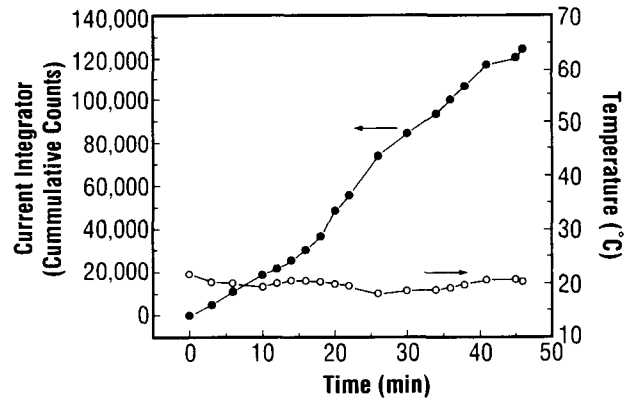

Figure 13d. Total flux and temperature plotted against total time for the 2×10^{17} H^+/cm^2 implant using the current integrator to monitor dosage. Although this implant took days, both the specimen temperature and accelerator output were maintained at a constant level.

After implantation, the silicon samples were removed from the diamond specimens. In order to cut the specimens into smaller pieces for further analysis, a diamond-tipped scribe pen was used to mark the backside of the wafers. The silicon samples would cleave along the mark, but the diamond samples, more often than not, would only partially break along the scribe; moreover, in the heavily irradiated diamond specimen, the film would often delaminate from the substrate during cleavage. The end result was that less suitable material was available for further analysis.

4.1 Visual Examination

The visual examination revealed that, in the 2×10^{15} H^+/cm^2 implantation, there were no visible changes in the diamond or silicon specimens. For the 2×10^{16} H^+/cm^2 specimens, a mark was made on the surface of the specimen to delineate the irradiated area. While the diamond specimen was noticeably darker, the silicon specimen showed little visible change. Both of the 2×10^{17} H^+/cm^2-implanted specimens were visibly much different from the as-deposited samples. The implantation severely darkened the surface of the diamond specimen. Two areas appear significantly browner in color than the remainder of the wafer, and the diameter of the beam is clearly visible. The silicon sample turned dark blue as a result of the implantation. A composite photograph of all the specimens after each implantation regime is presented in figure 14.

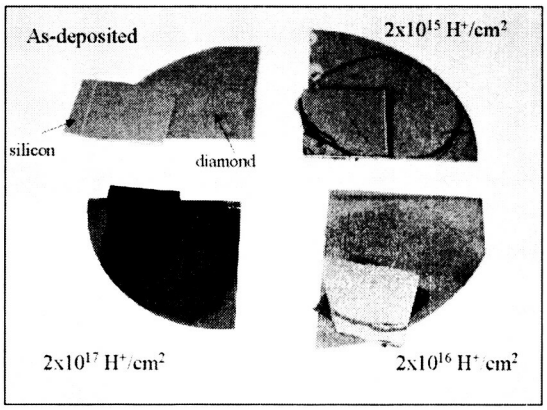

Figure 14. Photograph showing all specimens used in this investigation. The silicon samples are taped to the surface of the diamond to ensure equal implantation dosages. The black lines on two of the samples were used to outline the beam diameter.

4.2 Scanning Electron Microscopy—Diamond Top Surface

SEM analysis was performed on all unmounted specimens, examining the top surfaces and the cross-sectioned edges. Prior to SEM analysis, all samples were rinsed with acetone, which was immediately blown off with compressed air. However, debris remained on the surface of all specimens. This debris was examined by x-ray fluorescence spectroscopy and was identified as being composed of elements, such as calcium, potassium, and sulfur, although qualitative determination was not possible. Since the debris was present on all specimens, the material could not have been introduced via the implantation process. Also, this debris was absent on SEM analysis of the edge of the diamond specimens. As such, this debris was classified as surface contamination only. The top surface of the as-deposited diamond specimen indicated a <111> crystal growth with large facets. The grains are on the order of several microns in diameter with sharp, well-defined edges. Wide-angle and closeup views are presented in figure 15.

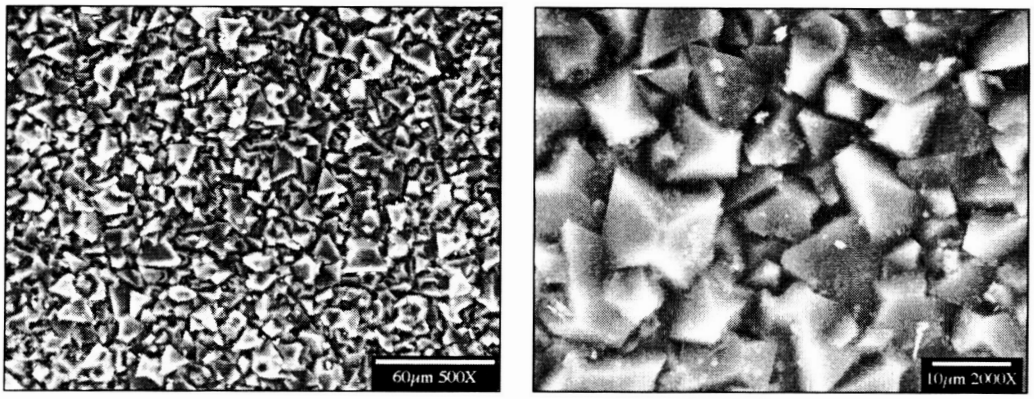

(a) (b)

Figure 15. SEM of the top surface of the as-deposited polycrystalline diamond film: (a) Wide-angle and (b) closeup.

The top surface of the 2×10^{15} H^+/cm^2-implanted specimen appeared to be identical to the as-deposited material. No visible change in the surface of the diamond was detected. Micrographs of this material are shown in figure 16. This SEM observation is consistent with the visual observation of the specimens immediately after irradiation.

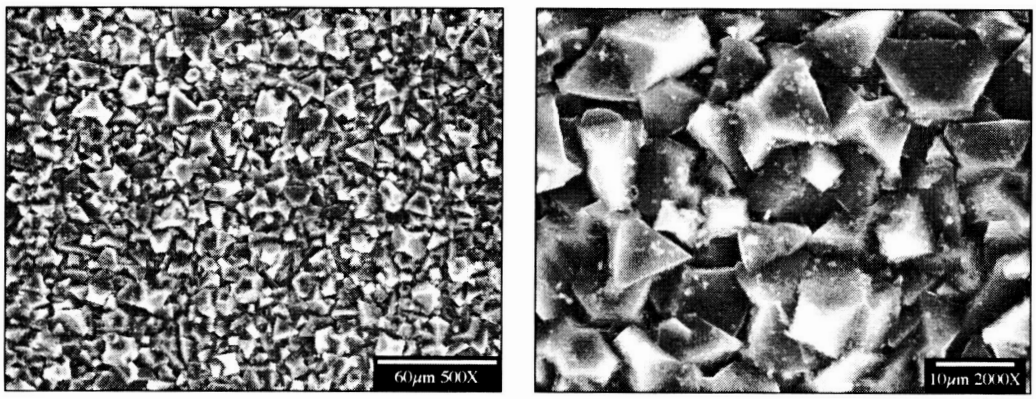

(a) (b)

Figure 16. SEM of the top surface of the 2×10^{15} H^+/cm^2-proton-implanted polycrystalline diamond film: (a) Wide-angle and (b) closeup.

Careful inspection of the top surface of the 2×10^{16} H^+/cm^2-implanted specimen indicated that although the crystallites remained intact, dark regions randomly populate the micrograph. However, the edges of the crystals remained well defined. These micrographs are shown in figure 17.

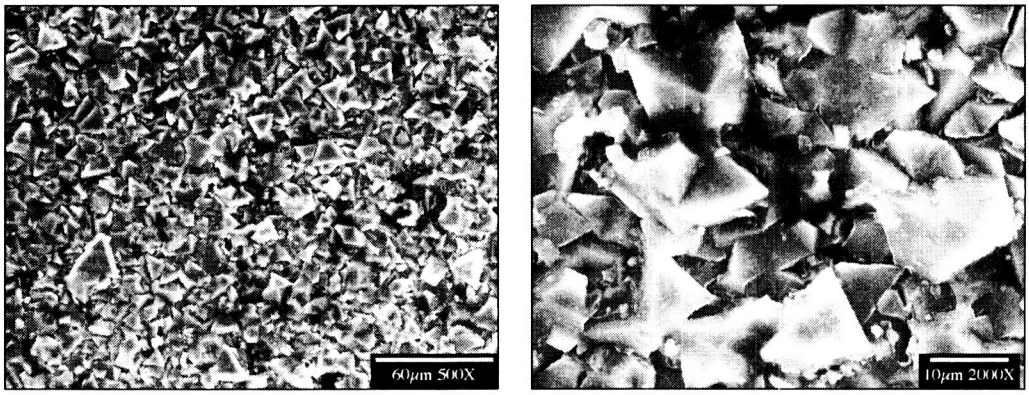

(a) (b)

Figure 17. SEM of the top surface of the 2×10^{16} H^+/cm^2-proton-implanted polycrystalline diamond film: (a) Wide-angle and (b) closeup.

The situation is significantly different for the 2×10^{17} H^+/cm^2-implanted materials, being the most heavily irradiated specimens. The wide-angle and closeup micrographs indicate severe degradation of the crystallite edges. The grains are so degraded that they have a somewhat melted appearance (fig. 18).

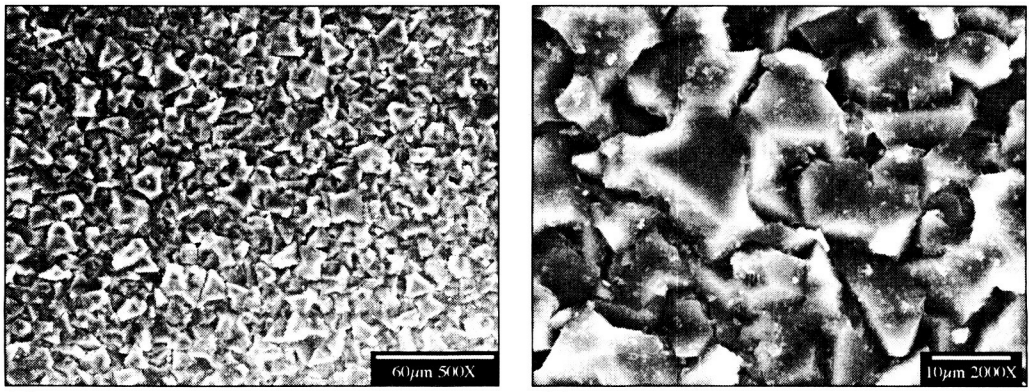

(a) (b)

Figure 18. SEM of the top surface of the 2×10^{17} H^+/cm^2-proton-implanted polycrystalline diamond film: (a) Wide-angle and (b) closeup.

Negative images of the SEM micrographs of the top surface of the as-deposited and 2×10^{17} H^+/cm^2-implanted diamond films samples are shown in figure 19. From this perspective, the damage to the surface is more readily observed. The grain edges are frayed and irregular as opposed to being sharp and uniform in the as-deposited samples.

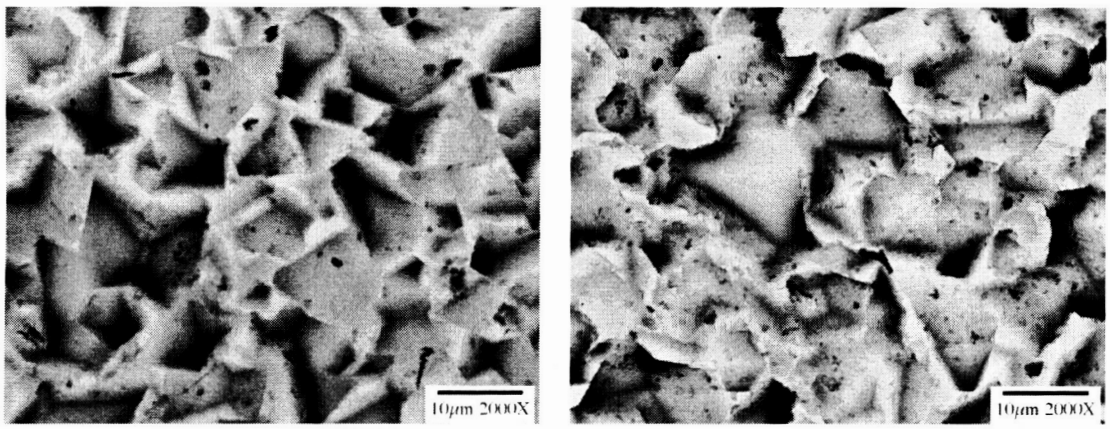

(a) (b)

Figure 19. Negative images of SEM micrographs of: (a) The as-deposited and (b) the heavily irradiated diamond material.

4.3 Micro-Raman Analysis—Diamond Top Surface

Raman spectra were collected in triplicate from the top surface of each specimen and are presented in figures 20 and 21. While the penetration depth of the Raman laser signal varies with opacity, surface roughness, laser energy, etc., the signal does penetrate several microns into the material. The spectra have been averaged, smoothed, and normalized. A Lorentzian function was used for curve fitting and an example is shown in the inset of figure 20(a) for the as-deposited spectra. Single-crystal diamond exhibits a sharp Raman peak at ≈1,333 cm^{-1} with a full width at half maximum (FWHM) of <3 cm^{-1} with no other spectral signatures present. As indicated in figure 20(a), the as-deposited material compared extremely well with high-purity, single-crystal material, although the diamond used in this study was polycrystalline. The diamond peak is sharp, well defined, and symmetrical. The FWHM is close to that reported for high-purity, single-crystal material (≈3 cm^{-1}). No graphitic or amorphous bands are observed.

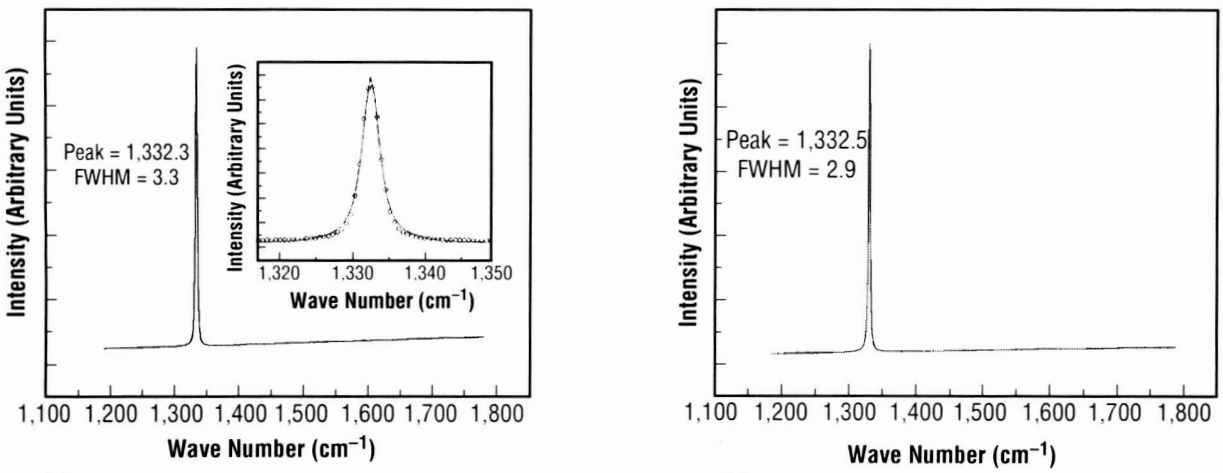

(a) (b)

Figure 20. Micro-Raman spectra of the top surface of: (a) The as-deposited polycrystalline diamond wafer with an inset that shows Lorentzian fit to experimental data, and (b) the 2×10^{15} H^+/cm^2-implanted polycrystalline diamond wafer.

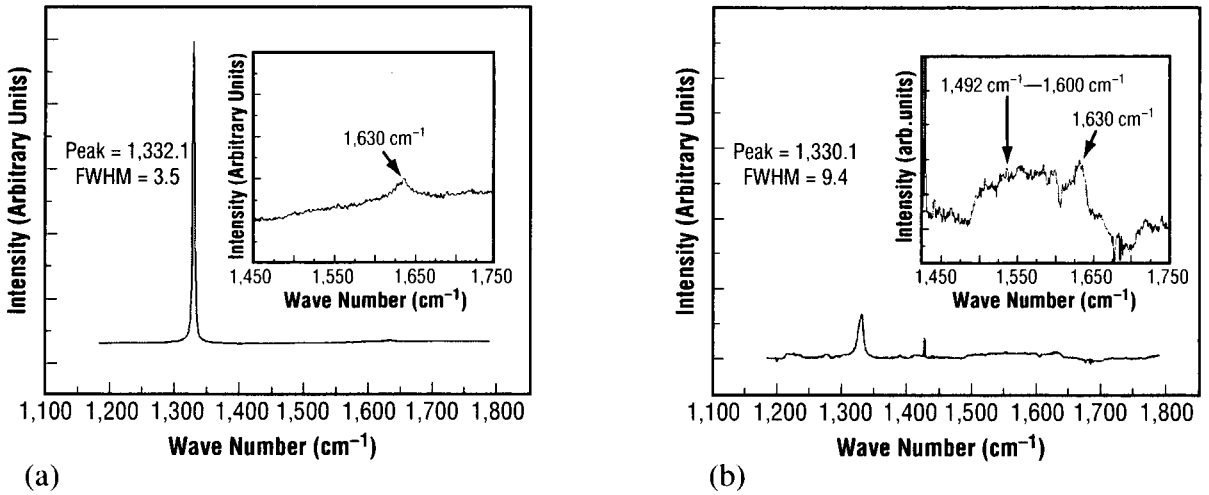

Figure 21. Micro-Raman spectra of the top surface of: (a) The 2×10^{16} H^+/cm^2-implanted polycrystalline diamond wafer with an inset that shows implantation-induced damage, and (b) the 2×10^{17} H^+/cm^2-implanted polycrystalline diamond wafer with an inset that shows implantation-induced damage.

The Raman spectra for the diamond specimen that was irradiated with a proton dose of 2×10^{15} H^+/cm^2 compared favorably with the as-deposited material. The FHWM was slightly lower but within the experimental error for the as-deposited sample. No graphitic components were detected. The diamond peak is sharp, well defined, and symmetrical, indicating no measurable microstructural damage from the irradiation. The intensity of the peak very closely matched the intensity of the as-deposited specimen.

The Raman spectra from the top surface of the 2×10^{16} H^+/cm^2 implant show some effects of the implantation. Since a slight amount of darkening is present in this sample, the probe depth of the laser is reduced with respect to the as-deposited and 2×10^{15} H^+/cm^2-implanted samples. While the diamond peak is sharp, intense, and largely symmetrical, the peak is shifted slightly downward, indicating tension within the microstructure. The slight increase in the FWHM, taken with the 1,630 cm^{-1} peak (clearly evident in the fig. 21(a) insert) suggests that ion-induced defects are responsible.

The spectra taken from the top surface of the most heavily irradiated specimen indicate extensive ion-induced damage to the microstructure. Due to the extreme darkening of the surface of this specimen, the probe depth of the Raman signal is attenuated in comparison to the as-deposited and 2×10^{15} H^+/cm^2-implanted samples. The first-order diamond peak is shifted downward by almost two wave numbers, and the intensity of the peak is greatly diminished. The FWHM broadening is due to the ion-induced defects that are observed from approximately 1,490 to 1,650 cm^{-1}. Peaks attributed to ion-implantation damage; i.e., the monovacancy at 1,490 cm^{-1}, the split interstitial at 1,630 cm^{-1}, and the broad graphitic band at $\approx$1,550 cm^{-1}, are observed. Other damage-related peaks are also observed; however, the sharp line located at $\approx$1,430 cm^{-1} is due to a detector malfunction within the Raman system.

Figure 22 presents an overview of the top-surface micro-Raman investigation. The first-order Raman peak position and the first-order peak FWHM are examined in relationship to proton dosage.

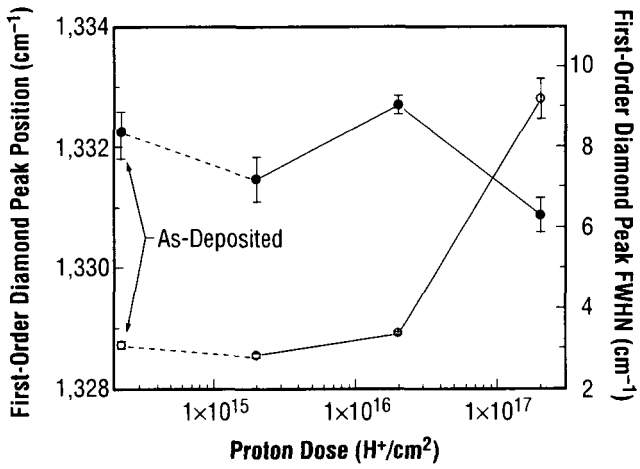

Figure 22. Graph showing first-order diamond peak position and first-order diamond peak FWHM as a function of proton dosage.

With respect to the first-order diamond peak position, within experimental error, the as-deposited and 2×10^{15} H^+/cm^2-implanted specimens are very similar to each other. The 2×10^{16} H^+/cm^2- and 2×10^{17} H^+/cm^2-implanted samples reveal increasing damage with increasing proton dosage. However, the first-order diamond peak was still evident. This is not surprising since the greatest amount of microstructural damage is expected to occur near the end of range (EOR) of the implant, which in this case is ≈4 μm deep, and not near the surface of the material where the majority of the Raman signal originates from within the sample.

The FWHM follows a similar pattern for this series of implantations. The as-deposited and 2×10^{15} H^+/cm^2 implants were, within experimental error, unaffected by the irradiation. The 2×10^{16} H^+/cm^2 implant reveals a slight broadening, indicating microstructural damage, and the 2×10^{17} H^+/cm^2 implant indicates a much larger shift.

4.4 Scanning Electron Microscopy Analysis—Diamond Cross Section

After SEM analysis of the top surfaces of the diamond specimens, SEM analysis was performed along the fractured edges of the diamond specimens. This was done in order to visually examine any depth-dependent effects the proton implantation might have created. Based on TRIM calculations, the protons were expected to penetrate ≈4 μm into the diamond specimen. The results of this investigation are shown in figures 23–25.

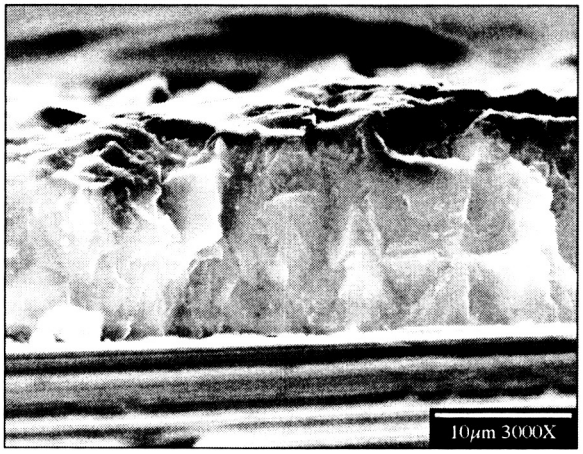

(a)

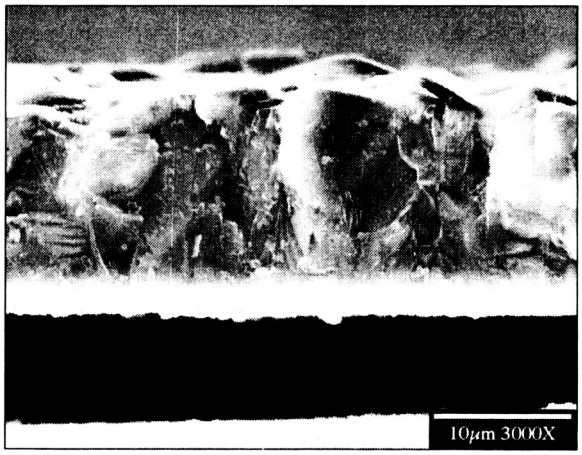

(b)

Figure 23. SEM micrograph showing the edge surface of: (a) The as-deposited polycrystalline diamond wafer with the diamond film/silicon substrate interface indicated by the white horizontal line near the lower portion of the figure, and (b) the 2×10^{15} H^+/cm^2-implanted polycrystalline diamond wafer.

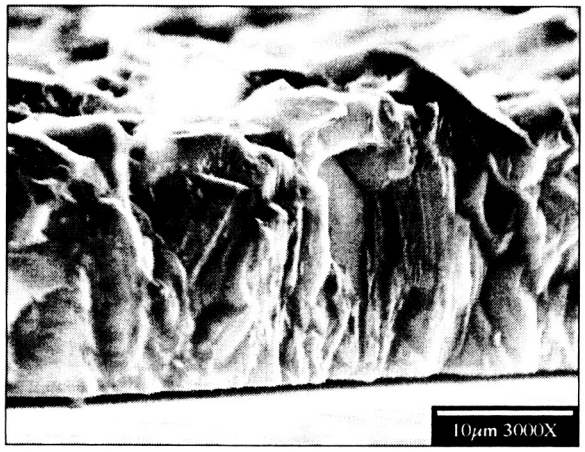

Figure 24a. SEM micrograph showing the edge surface of the 2×10^{16} H^+/cm^2-implanted polycrystalline diamond wafer.

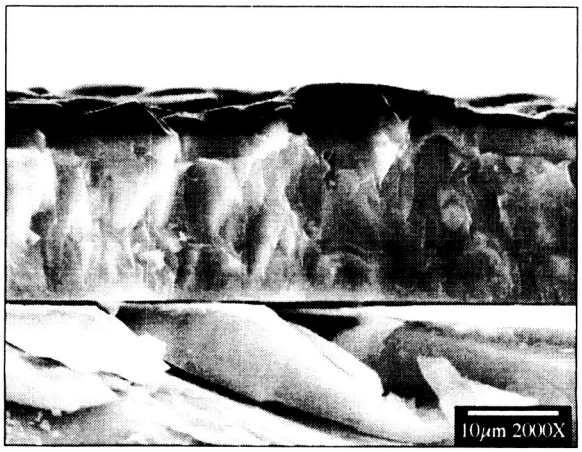

Figure 24b. Wide-angle SEM micrograph showing the edge surface of the 2×10^{17} H^+/cm^2-implanted polycrystalline diamond wafer. The film/substrate interface is seen in the lower half of the figure.

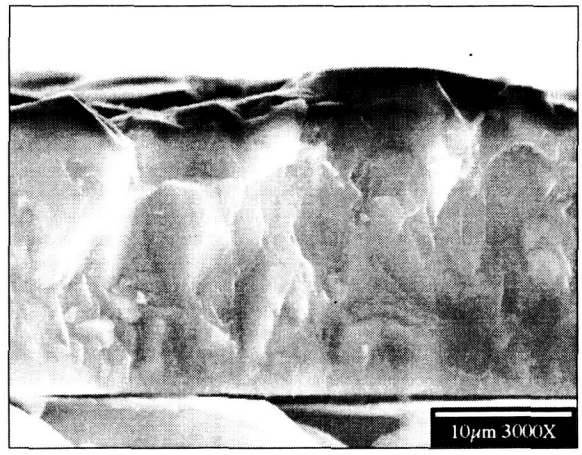

Figure 25. Closeup SEM micrograph showing the edge surface of the 2×10^{17} H^+/cm^2-implanted polycrystalline diamond wafer.

SEM cross-section analysis of the as-deposited material revealed an extremely rough edge surface. The analysis also revealed that the interface of the diamond film/silicon substrate is clearly evident. Columnar grain growth, typically seen in <111> diamond films, is difficult to detect in this specimen.

The 2×10^{15} H^+/cm^2-implanted film edge looks much like the as-deposited material. In figure 23(b), the diamond film has delaminated from the substrate and protrudes upwards. This results in the black area below the diamond film. No change in the appearance of the film, as a function of depth, from the edge surface is observed.

The edge of the 2×10^{16} H^+/cm^2-implanted film is shown in figure 24(a). Once again, the interface between the diamond and silicon substrate is evident in the lower portion of the micrograph. No radiation damage, either on the surface or down the edge, is observed.

Figure 24b presents a wide-angle view of the edge of the 2×10^{17} H^+/cm^2-implanted film. The silicon substrate is absent from the diamond film-silicon interface but is seen in the background, and this results in the film overhanging the substrate. The top of the surface of the diamond film is darker than in the preceding micrographs. The edge surface is rough; however, near the top of the edge, the surface appears smoother than the remainder of the cross section. The width of this layer corresponds with the expected range of the proton-implantation EOR.

Figure 25 is a closeup SEM micrograph of the cross section shown in figure 24b. The upper portion of the edge surface, containing the region that received the implanted protons, appears to possess the same texture as the deeper layers in the film that did not receive radiation damage. This specimen possesses a large surface roughness, which was evident in all four specimens.

Figure 26 presents a side-by-side comparison of the cleaved edges of the as-deposited and heavily irradiated diamond films using negative images of the SEM micrographs. The surface and upper portion of the most heavily irradiated diamond films appear very similar with respect to the reference material. Swelling has been reported in heavily irradiated diamond material, and a slight amount of swelling appears to be present in this specimen.

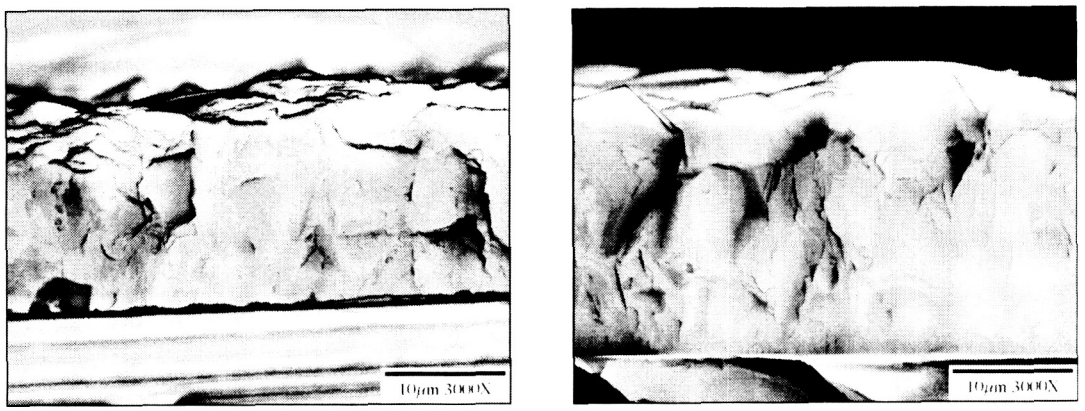

(a) (b)

Figure 26. Negative images of SEM micrographs of: (a) The as-deposited polycrystalline diamond film and (b) the 2×10^{17} H^+/cm^2-implanted polycrystalline diamond film.

4.5 Micro-Raman Analysis—Diamond Cross Section

Raman spectra were obtained on unpolished and polished diamond specimens. No artifacts from the polishing were observed, and since the polished specimens did provide a more uniform surface for investigation, they were used for the high-resolution data collection. Figure 27 shows, schematically, the sample configuration used throughout the analysis for the diamond and silicon specimens.

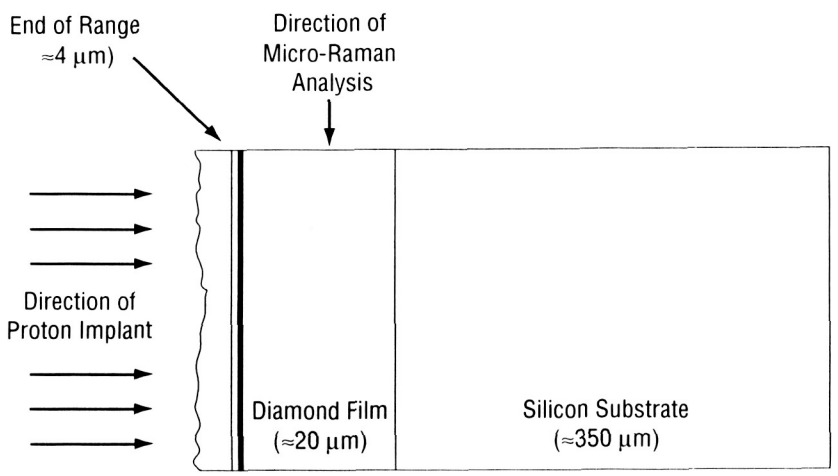

Figure 27. Schematic illustrating the direction of proton implantation and specimen orientation for the micro-Raman cross-sectional analysis.

The micro-Raman spectra were collected by performing a line scan across the specimen cross section. Each line scan consisted of 40 individual spectra that were collected at intervals of 1 μm. The scan started on the silicon substrate and finished past the edge of the sample. Since silicon and diamond have very different Raman signatures, locating the interfaces of the films was relatively simple, but this was complicated by the fact that near the films' interfaces, the Raman spot size included contributions from both the silicon and diamond.

The spectra for the as-deposited material is shown in figure 28(a). The 1 μm line scan contains a sharp first-order diamond peak at ≈1,332 cm^{-1}. However, the broad band from approximately 1,450 to 1,700 cm^{-1} is indicative of graphitic-like carbon. This is attributed to surface effects, where carbon exists in a variety of bonding configurations. The 2- to 6-μm scans are void of this broad peak, signifying the high fidelity of the carbon film throughout the entire layer. This material appears to be free of depth-dependent stress and microstructural damage due to the fact that the first-order diamond peak shifted very little and there was not an increase in the FWHM.

The 2×10^{15} H^+/cm^2-implanted specimen is shown in figure 28(b) and looks similar to the control specimen. The graphitic band extends to the second line scan in this material. This is likely due to uncertainty in calibrating exactly where the edge to the diamond film is located and, since the Raman probe is ≈1 μm in diameter, error in spatial resolution. This, of course, was a factor in all of the cross-sectional Raman examinations. The absence of any shift or increase in the first-order diamond line indicates no measurable effect caused by the proton implantation. Most importantly, no implantation damage is observed in the regions where damage should be evident; i.e., in the 1,490, 1,550, and 1,630 cm^{-1} regions in the subsurface of the films.

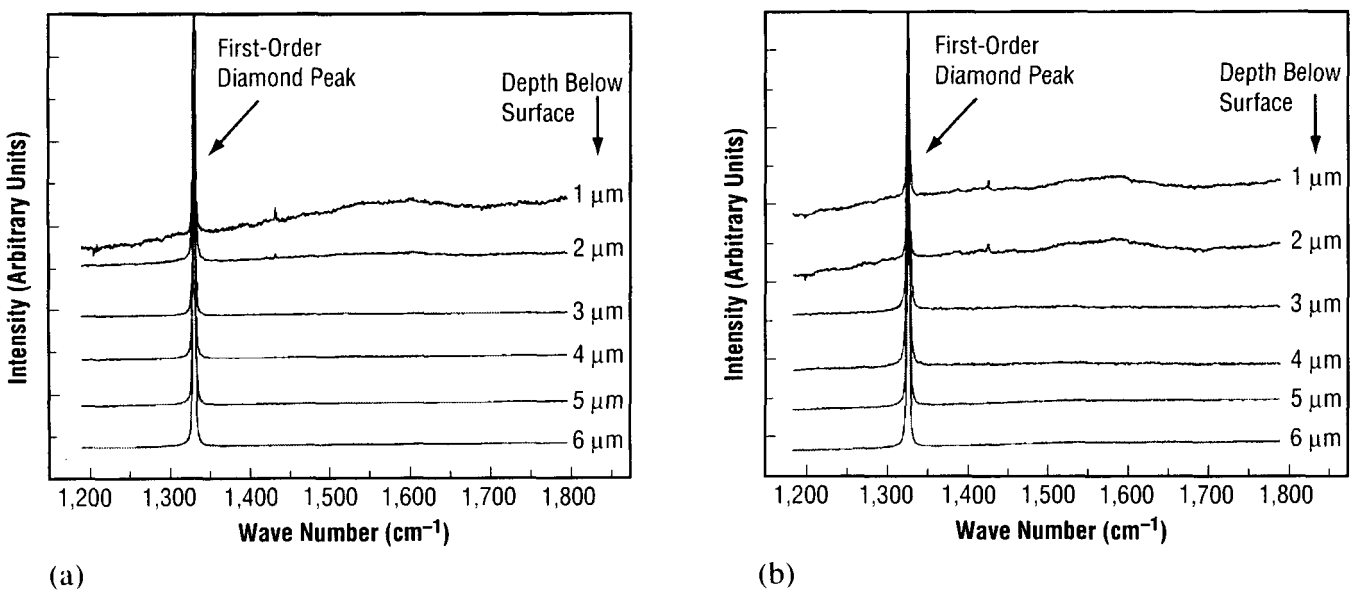

Figure 28. Micro-Raman spectra as a function of depth across the surface of: (a) The as-deposited polycrystalline diamond film and (b) the 2×10^{15} H^+/cm^2 polycrystalline diamond film.

The depth-dependent micro-Raman line scans for a representative specimen of the 2×10^{16} H^+/cm^2 implantation are presented in figure 29. Even in the 1-μm scan, a defect-related peak is observed at 1,630 cm^{-1}. This defect is associated with the <100> split interstitial. This peak increases with depth and reaches a maximum at 4 μm, beyond which it decreases rapidly, and it is absent at 6 μm. Also, there is a slight increase in the baseline between 1,400 cm^{-1} and the 1,630 cm^{-1} peak. This indicates amorphous-type material, and it is the first detected in the irradiated specimens.

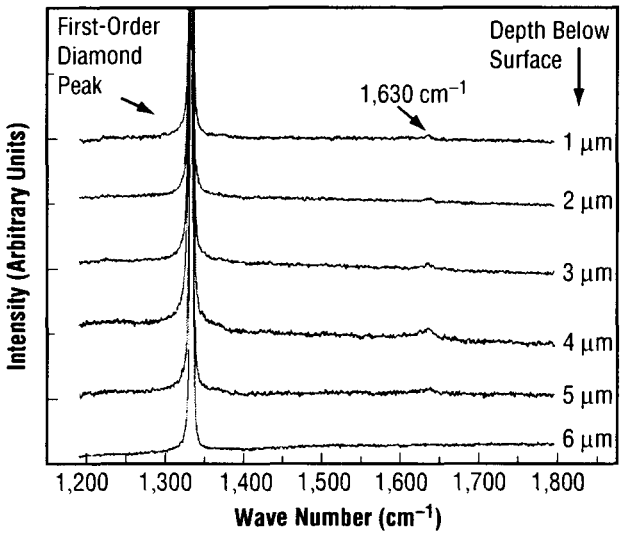

Figure 29. Micro-Raman spectra as a function of depth across the surface of the 2×10^{16} H^+/cm^2 polycrystalline diamond film.

Further insight regarding the depth-dependent effects of the 2×10^{16} H^+/cm^2 implant can be observed by examining the first-order peak position and first-order diamond peak FWHM as a function of depth. This is presented in figure 30 for four replicate analyses. A downward shift of the first-order peak occurs rapidly from the surface to 4 μm, where the shift then begins to decrease until reaching a constant at ≈10 μm. Similarly, the first-order diamond FWHM rapidly increases until reaching a maximum at 4 μm, where it also declines until reaching a constant at ≈10 μm. These data indicate that the film is under tension and exhibits microstructural damage as well.

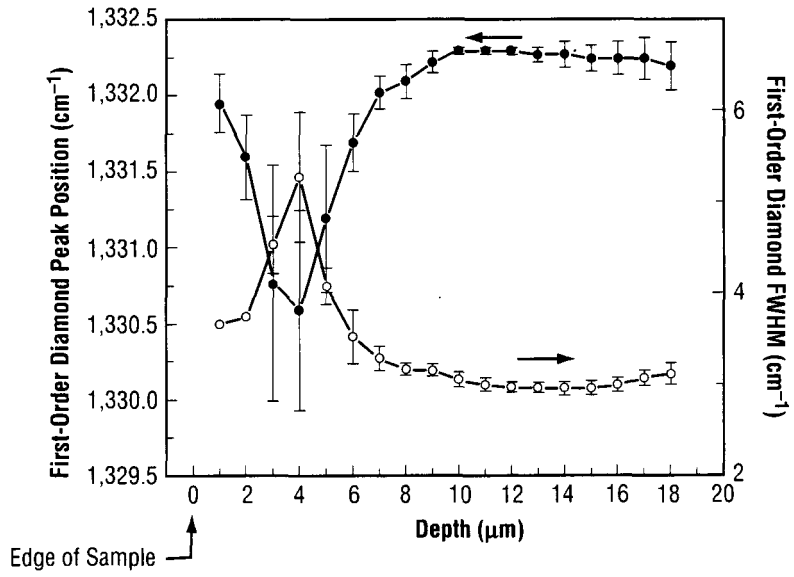

Figure 30. Analysis of the first-order diamond peak position and first-order diamond FWHM as a function of cross-sectional depth in the 2×10^{16} H^+/cm^2-irradiated polycrystalline diamond film.

The proton implantation effect as a function of depth for the most heavily irradiated specimen, the 2×10^{17} H^+/cm^2 implant, is presented in figure 31. In this representative line scan series, extensive defect-related spectral signatures are evident, even at 1 μm. The vacancy at 1,495 cm^{-1}, the broad amorphous region at ≈1,550 cm^{-1}, and the <100> split interstitial at 1,630 cm^{-1} are all present. The first-order Raman line is greatly diminished in intensity as compared to the control sample. The damage increases until reaching a maximum at 4 μm. At this depth, the diamond peak is diminished in intensity but still present. The 1,495-cm^{-1} peak may be present, but resolution is impossible due to the baseline increase that is present throughout this region. The 1,630-cm^{-1} peak also grows in intensity, as a function of depth, until reaching a maximum at 4 μm. At a depth of 6 μm, the spectra returned to looking very similar to the as-deposited specimen, although the baseline is still slightly elevated across the entire 1,400- to 1,650-cm^{-1} region.

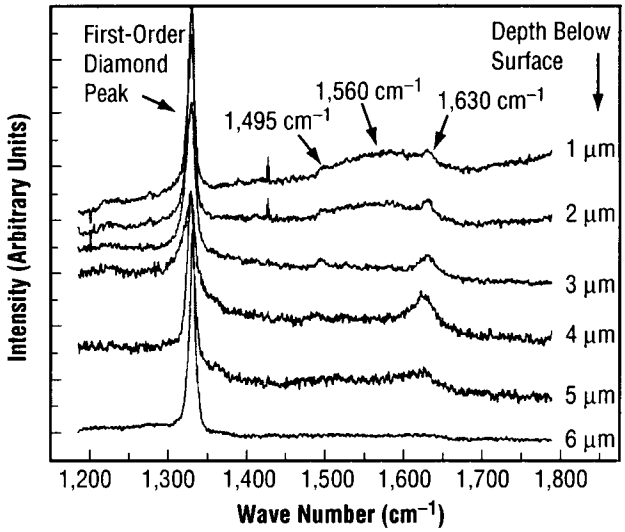

Figure 31. Micro-Raman spectra as a function of depth across the surface of the 2×10^{17} H^+/cm^2 polycrystalline diamond film.

Curve fitting was employed to examine, in detail, the damaged region in the spectra shown in figure 31. As seen in figure 32, implantation-related defects are observed at 1,495 cm^{-1} for the vacancy, 1,580 cm^{-1} for amorphous carbon, and at 1,630 cm^{-1} for the <100> split interstitial. Throughout the entire cross section, the 1,630-cm^{-1} peak rapidly increased in intensity until reaching the EOR while the 1,495-cm^{-1} peak remained constant or diminished until reaching the EOR.

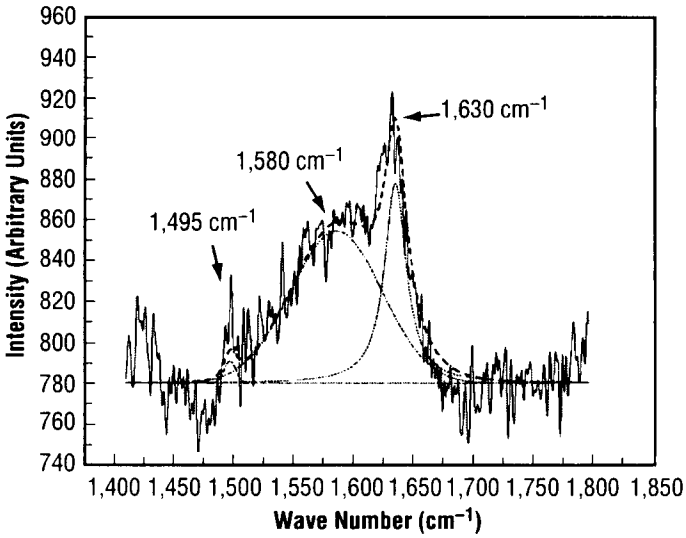

Figure 32. Representative spectra detailing the curve fitting used to examine the damaged region in the 2×10^{17} H^+/cm^2-implanted diamond film.

The first-order diamond peak position and first-order diamond FWHM as a function of depth are shown in figure 33a, and the comparison of the first-order diamond peak position as a function of first-order diamond peak FWHM at ≈4 μm in depth is shown in figure 33b. The behavior of the peak-position shift is very similar to the 2×10^{16} H^+/cm^2-implanted specimen although greater in magnitude. The same is true for the FWHM behavior. Again, the surface appears to be under tension and contains implantation-induced microstructural damage.

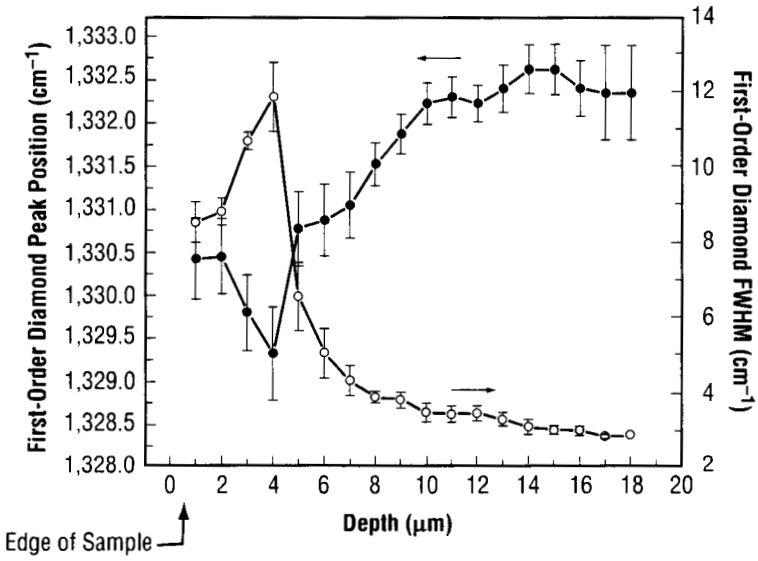

Figure 33a. Analysis of the first-order diamond peak position and first-order diamond FWHM as a function of cross-sectional depth in the 2×10^{17} H^+/cm^2-irradiated polycrystalline diamond film.

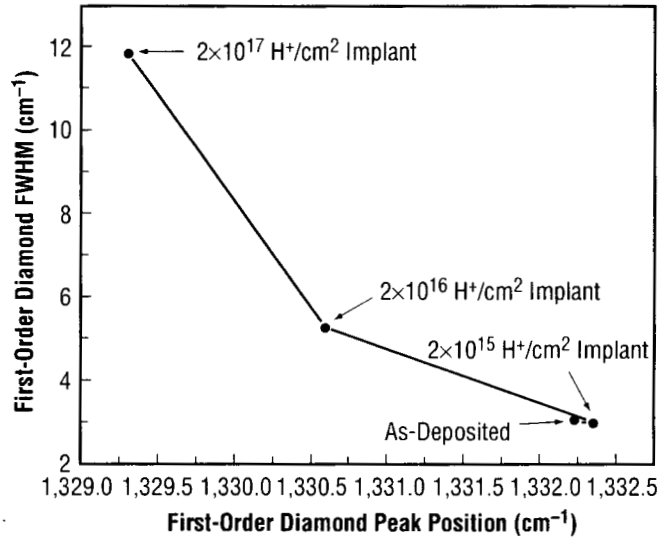

Figure 33b. Comparison of the first-order diamond peak position as a function of first-order diamond peak FWHM at ≈4 μm in depth, near the EOR for the proton implantation.

An examination of the first-order peak-position shift and first-order diamond peak FWHM at the EOR for the entire diamond series is presented in figure 34. These graphs show that the effects of proton implantation increased in an almost exponential manner with increasing proton dose and that no effect of the implant was observed in the 2×10^{15} H^+/cm^2 dosed specimen.

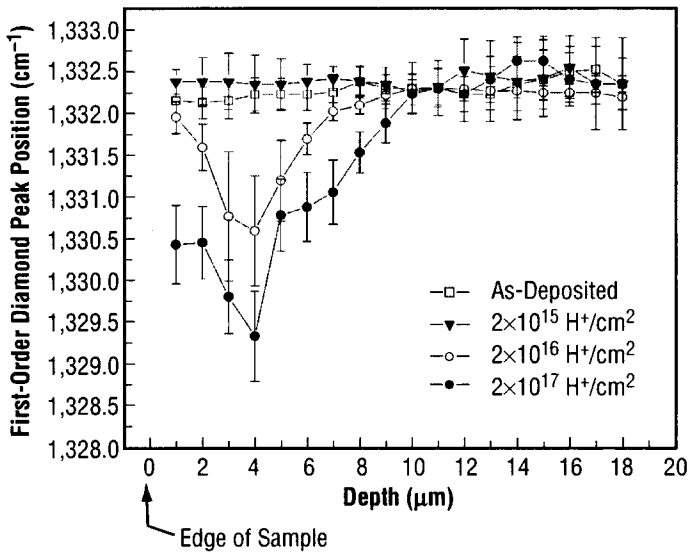

(a)

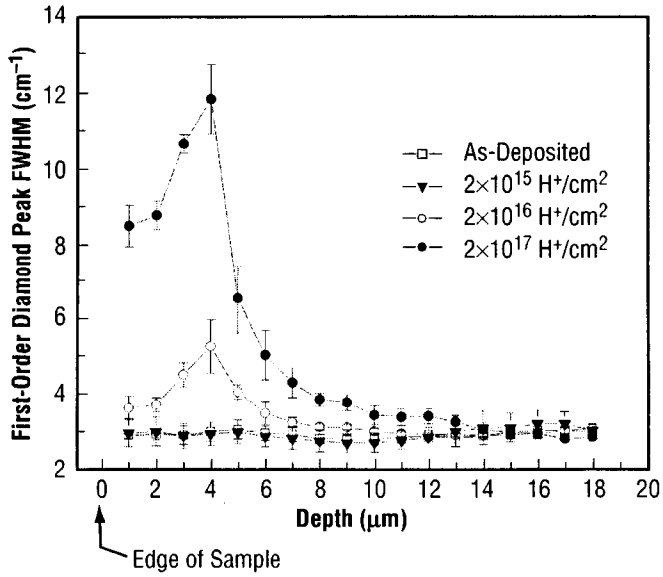

(b)

Figure 34. Summary chart for the entire implantation series showing the variation in: (a) The first-order peak position as a function of depth and (b) the first-order FWHM as a function of depth.

A summary graph of the first-order diamond peak position as a function of depth is presented in figure 34(a). No effects, within experimental error, are observed in the 2×10^{15} H^+/cm^2 implant at any depth. However, the 2×10^{16} H^+/cm^2 and 2×10^{17} H^+/cm^2 dosages caused measurable shifts in the first-order diamond peak position, although at 10 μm, both specimens had returned to as-deposited peak-position values. The unexpected slow return to the baseline is examined in section 5 of this Technical Memorandum.

In a similar fashion, the first-order diamond peak FWHMs for all the implantation regimes are presented in figure 34(b). Again, no apparent effects from the implantation are observed for the 2×10^{15} H^+/cm^2 implant. The 2×10^{16} H^+/cm^2 and 2×10^{17} H^+/cm^2 FWHMs increased rapidly until reaching the EOR and then decreased slowly until ≈10 μm, where the values then returned to baseline behavior as in the control specimen.

4.6 Scanning Electron Microscopy Analysis—Silicon Top Surface

As with the diamond samples, the silicon specimens were first rinsed with acetone and then immediately dried with compressed air prior to SEM analysis. Surface contamination was present, although not nearly as severe as the contamination observed on the surface of the diamond material. Since contamination was detected in both materials, it is thought that perhaps the sample holders—plastic petri dishes—were responsible for the introduction of the foreign material.

The SEM micrograph of the as-deposited polycrystalline silicon top surface is presented in figure 35. The grain edges are not well defined, but on average, each grain is at least 10 μm or greater in size. Overall, the surface is rough, but individual grains exhibit smooth surfaces. Deep voids are present where grains intersect. The closeup SEM micrograph of the as-deposited material is shown in figure 35(b). (The white particulate is contamination.)

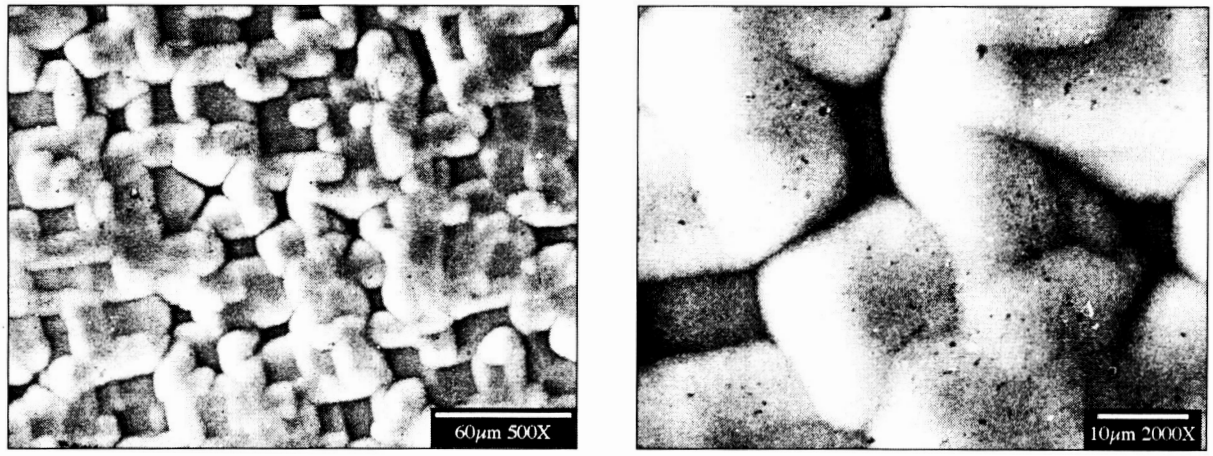

(a) (b)

Figure 35. SEM micrograph of the top surface of the as-deposited polycrystalline silicon wafer: (a) Wide-angle and (b) closeup.

Examination of the surface of the 2×10^{15} H^+/cm^2-implanted material revealed no visible damage due to the proton implantation. The surface in both the wide-angle and closeup micrographs appeared very similar to the nonirradiated material, and the micrographs are shown in figure 36.

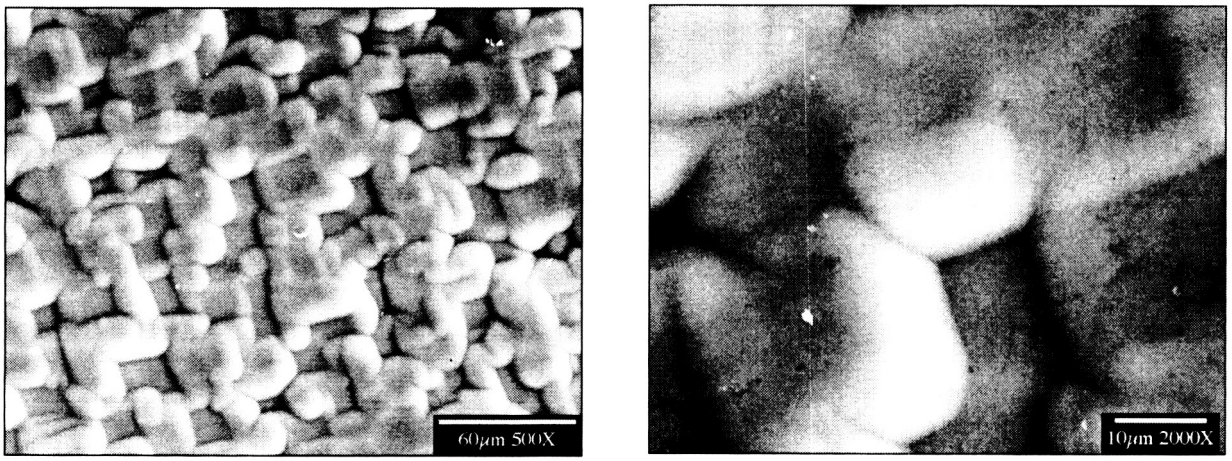

(a) (b)

Figure 36. SEM micrograph of the top surface of the 2×10^{15} H^+/cm^2-implanted polycrystalline silicon wafer: (a) Wide-angle and (b) closeup.

SEM examination of the top surface of the 2×10^{16} H^+/cm^2 implant was also very similar in appearance to both the as-deposited and 2×10^{15} H^+/cm^2 specimens. No crater-like features or differing texture was observed in either the wide-angle or closeup micrographs (fig. 37).

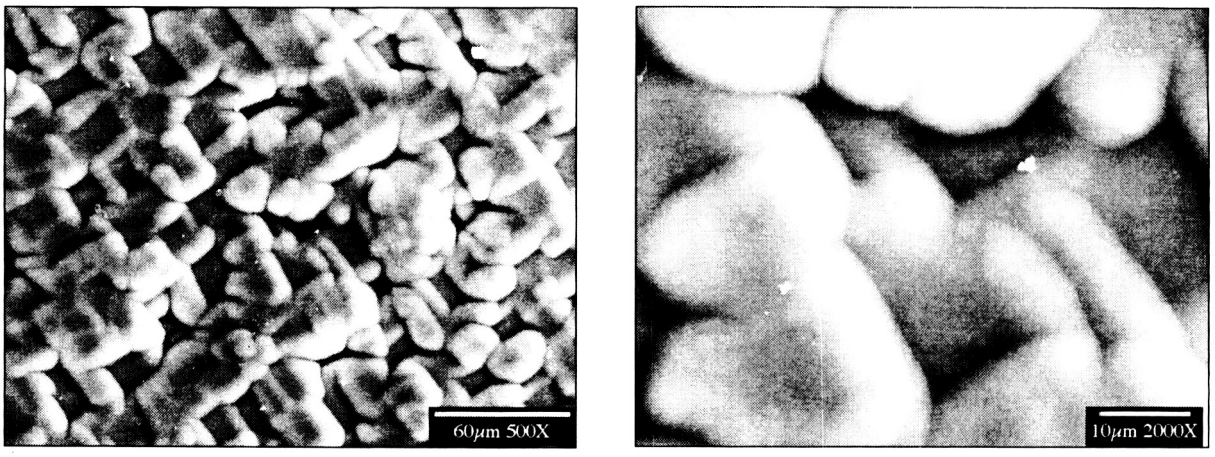

(a) (b)

Figure 37. SEM micrograph of the top surface of the 2×10^{16} H^+/cm^2-implanted polycrystalline silicon wafer: (a) Wide-angle and (b) closeup.

Figure 38 presents the SEM micrographs of the top surface of the 2×10^{17} H^+/cm^2 implant. They were also very similar in appearance to the other three specimens; however, overall, the surface appeared to be somewhat darker than the other specimens. The closeup micrograph was also devoid of any distinguishing implantation-induced surface features.

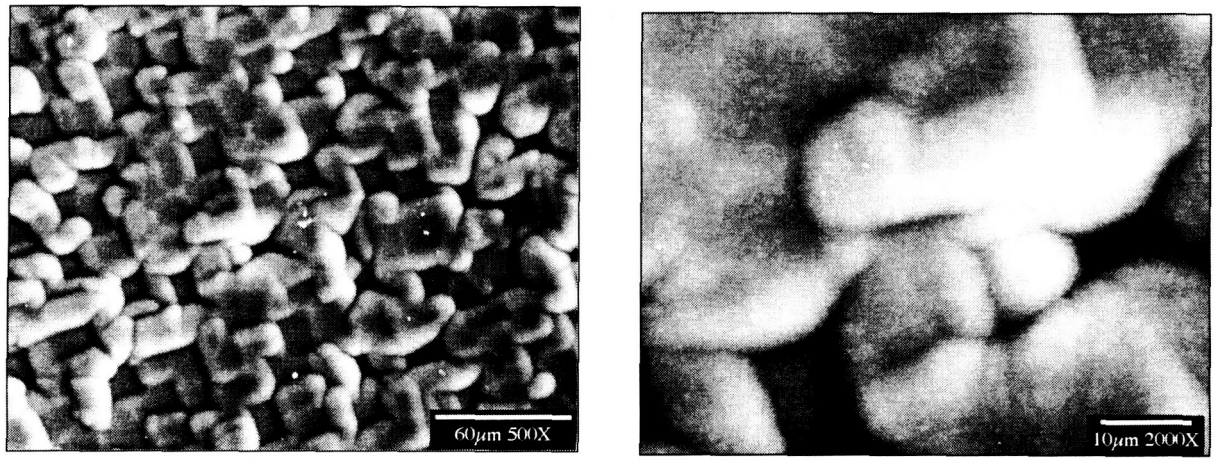

(a) (b)

Figure 38. SEM micrograph of the top surface of the 2×10^{17} H^+/cm^2-implanted polycrystalline silicon wafer: (a) Wide-angle and (b) closeup.

In order to provide additional insight into the differences between the as-deposited and heavily irradiated materials, negative images of the SEM micrographs were prepared and are presented in figure 39. Using this enhancement, the contrast in the surface layer of the silicon is more readily visible. Grain edges appear very similar in both micrographs, unlike that which was observed in the diamond series in which great contrast was observed between the control and heavily irradiated specimens.

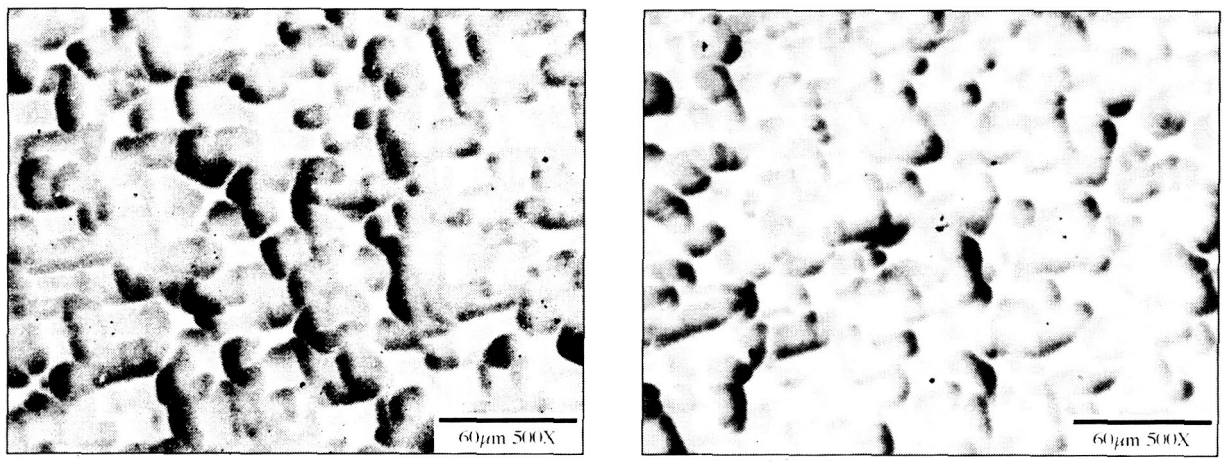

(a) (b)

Figure 39. Negative images of the wide-angle SEM micrographs of: (a) The as-deposited and (b) 2×10^{17} H^+/cm^2-implanted polycrystalline silicon films.

4.7 Micro-Raman Analysis—Silicon Top Surface

Crystalline silicon exhibits a sharp first-order Raman shift due to the well-defined wave vectors of the phonons. The peak is symmetrical with a frequency of ≈521 cm^{-1} and an FWHM of ≈3 cm^{-1}. The frequency of polycrystalline silicon is shifted downward due to the presence of grain boundaries and other imperfections during deposition. An asymmetrical broadening of the peak is also often observed due to phonon confinement. While the laser penetration depth is much less than what was observed in the diamond surface analysis, the depth is even more reduced due to the amorphous-like properties of the polycrystalline material. Completely amorphous silicon, which contains very small crystallites, creates a large downshift of the peak. The end result is a broad, weak peak located at ≈480 cm^{-1}. The Raman signatures from these materials are presented in figure 40.

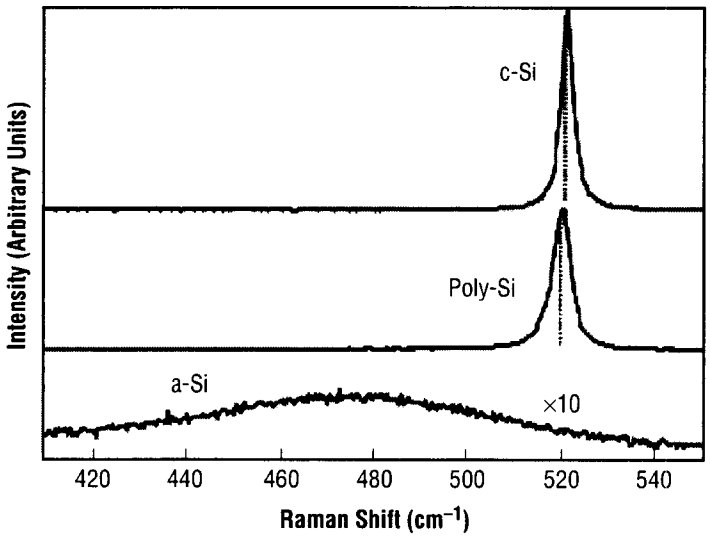

Figure 40. Typical Raman signatures from crystalline silicon (top), polycrystalline silicon (middle), and amorphous silicon (bottom).[30]

Raman spectra of the top surfaces of the polycrystalline silicon specimens were obtained in triplicate, then averaged. Peak fitting was performed using a Lorentzian function. Figure 41(a) contains the Raman spectra from the top surface of the as-deposited polycrystalline silicon film. The slight downward shift from ≈520 cm^{-1} and the large FWHM indicate that stress and microstructural defects are present in the film and were introduced during film deposition.

The Raman spectra of the 2×10^{15} H^+/cm^2-implanted specimen (fig. 41(b)) appeared to be very similar to the as-deposited sample. No visible effects of the irradiation were noted.

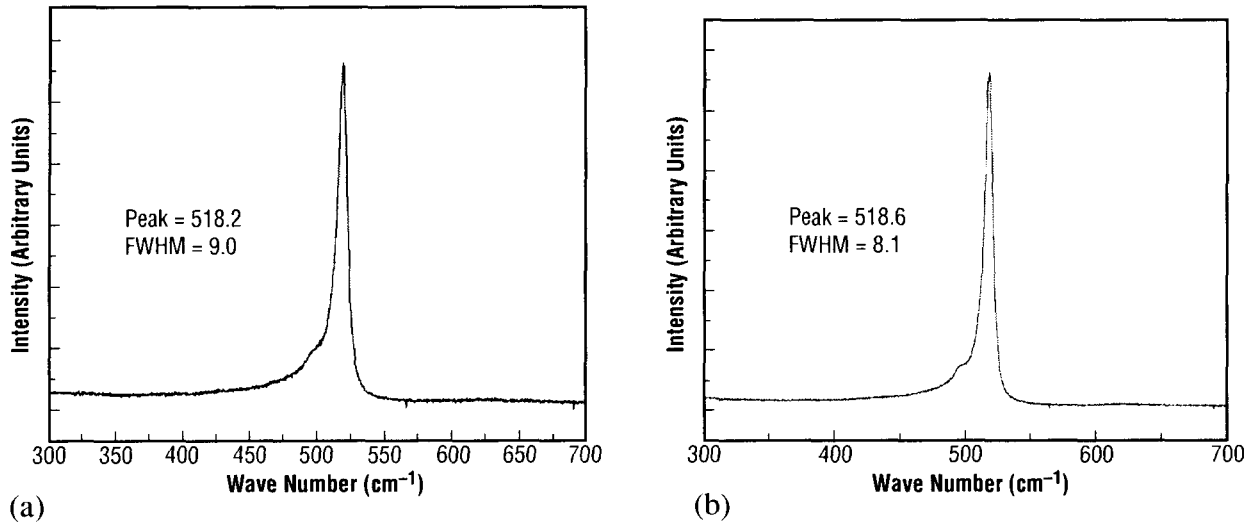

Figure 41. Micro-Raman spectra of the top surface of: (a) The as-deposited polycrystalline silicon wafer and (b) the 2×10^{15} H^+/cm^2-implanted polycrystalline silicon wafer.

The Raman spectra for the 2×10^{16} H^+/cm^2-implanted sample are presented in figure 42(a). Both the peak position and FWHM were within the experimental error of the as-deposited sample although the shoulder, located at $\approx$500 cm^{-1}, was slightly more pronounced.

The Raman spectra of the top surface of the most heavily irradiated specimen are presented in figure 42(b). The peak shift and FWHM broadening, while small, are consistent with implantation effects. A small amount of fluorescence was also observed in the raw spectrum and is consistent with the visual observations of the film after implantation. Also, compared to the other three specimens, the peak height was greatly diminished. Sample fluorescence could be partially responsible for this effect.

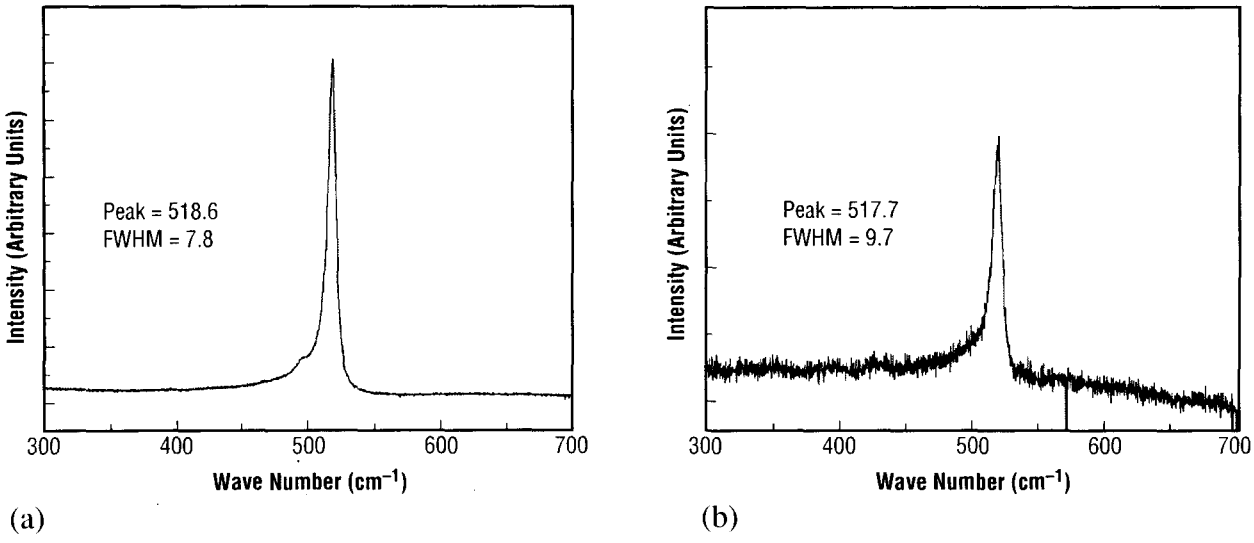

Figure 42. Micro-Raman spectra of the top surface of: (a) The 2×10^{16} H^+/cm^2-implanted polycrystalline silicon wafer and (b) the 2×10^{17} H^+/cm^2-implanted polycrystalline silicon wafer.

A summary of the Raman investigation of the top surfaces of the polycrystalline silicon films is presented in figure 43. Within experimental error, the silicon peak position remained constant in the as-deposited and 2×10^{15} H^+/cm^2- and 2×10^{16} H^+/cm^2-implanted samples. Even in the most heavily irradiated specimen, only a slight downward shift in peak position is observed. The FWHM behavior followed a very similar trend, returning to near-as-deposited values in the most heavily damaged material. Due to the wide variability in the density, grain distribution, and surface contour, the data set contains a large amount of deviation between points.

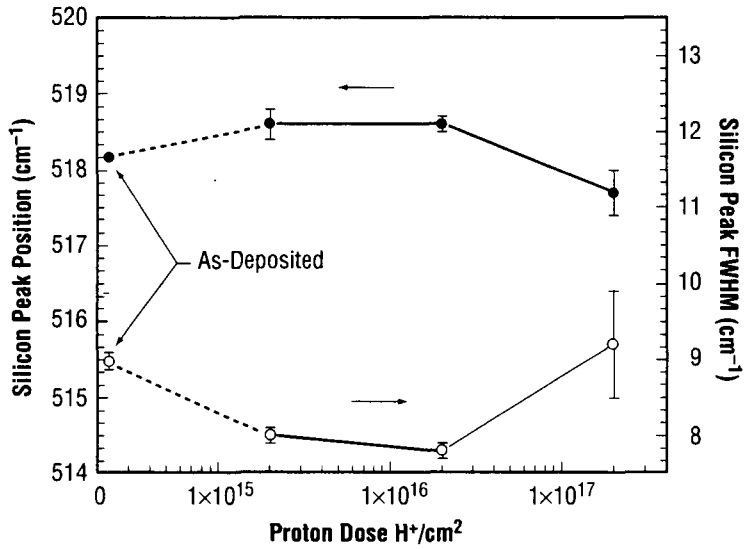

Figure 43. Polycrystalline silicon peak position and FWHM as a function of proton dosage for the entire silicon series.

4.8 Scanning Electron Microscopy Analysis—Silicon Cross Section

As with the diamond samples, the cross-sectioned silicon specimens were also examined via SEM along the cross section. The as-deposited silicon is shown in figure 44(a). The interface between the single-crystal silicon substrate and the polycrystalline silicon film is evident in the lower portion of the micrograph. The surface of the edge is somewhat smooth, although some significant regions of surface roughness are indicated by the dark areas.

TRIM calculations predicted that the protons would penetrate to a depth of ≈8 μm in the polycrystalline silicon. Examination of figure 44(b) indicated that the edge of the 2×10^{15} H^+/cm^2-implanted specimen appeared smooth with no visible effects of the implantation. Once again, the interface between the substrate and the film was evident in the lower portion of the micrograph.

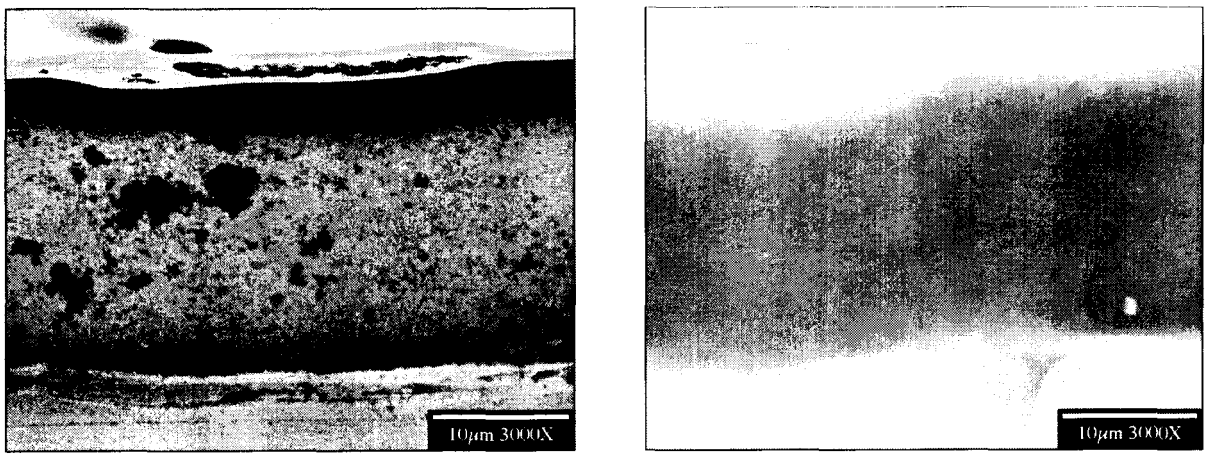

(a) (b)

Figure 44. SEM micrograph of the edge of: (a) The as-deposited polycrystalline silicon, with the interface between the polycrystalline silicon and single-crystal silicon evident in the lower portion of the micrograph and (b) the 2×10^{15} H^+/cm^2-implanted polycrystalline silicon sample with no noticeable effects of the implant. The interface between film and substrate is noticeable in the lower portion of the figure.

The SEM micrograph of the 2×10^{16} H^+/cm^2 implant is shown in figure 45. No observable effects of the proton implantation were detected. The interface between film and substrate is present. Debris, as indicated by the light-colored spots, was observed. The nonuniformity of the top surface is evident in figure 45.

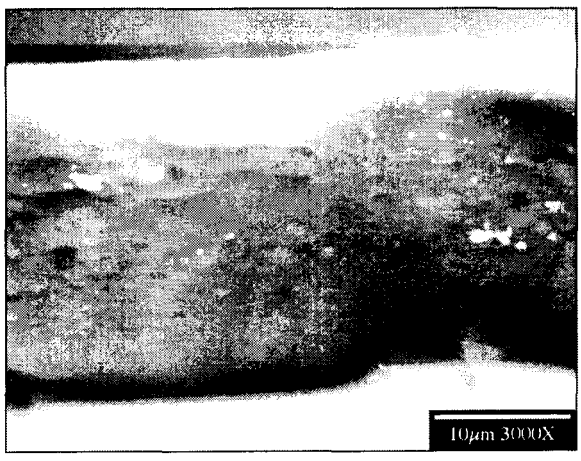

Figure 45. SEM micrograph of the edge of the 2×10^{16} H^+/cm^2-implanted polycrystalline specimen. No visible effects from the implantation are evident.

A wide-angle SEM view of the 2×10^{17} H^+/cm^2 implant is shown in figure 46(a). The white box in the micrograph encloses the polycrystalline thin film, and near the bottom, a portion of the single-crystal silicon substrate. This SEM micrograph indicates the presence of an interface running horizontally throughout the entire surface, ≈8 μm from the top surface. Figure 46(b) presents a detailed examination of the region outlined by the white box in 46(a). The interface, located ≈8 μm from the top surface, corresponds to the depth predicted by TRIM to be the EOR for the implanted protons. The interface appears to be quite narrow and closely follows the contour of the top surface of the film.

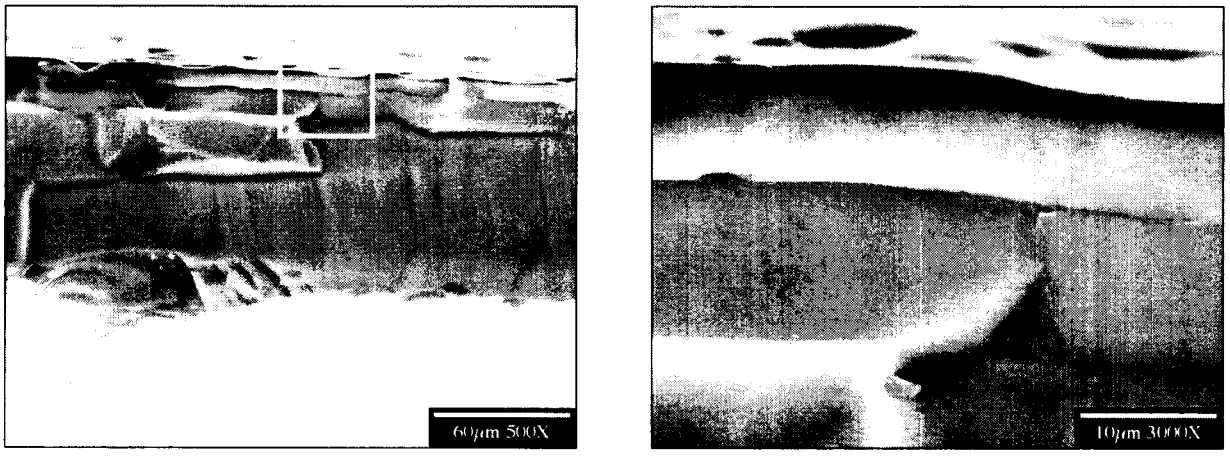

(a) (b)

Figure 46. SEM micrograph of the 2×10^{17} H^+/cm^2-implanted polycrystalline silicon: (a) Wide-angle—the polycrystalline silicon layer indicates an interface not seen in the other specimens and (b) closeup (outlined area, shown in greater detail)—an interface ≈8 μm from the top surface is clearly visible.

4.9 Micro-Raman Analysis—Silicon Cross Section

The unpolished silicon specimens were examined in the cross section via micro-Raman spectroscopy. The sample configuration and the number of scans were the same as those for the diamond specimens. Due to the nonuniformity of the silicon surface, which results in an inconsistent laser spot focus as evidenced in the SEM micrographs, there was a large amount of scatter in the data. This is evident in the data for the as-deposited silicon specimen shown in figure 47(a). Both the silicon peak position and FWHM exhibited a great deal of variability throughout the entire film depth. Additional factors that contribute to scatter in the data are the wide range of grain sizes and their orientations within the film.

The cross-sectional Raman data from the 2×10^{15} H^+/cm^2 implant also exhibited a high degree of variability in both the peak position and FWHM as a function of depth. However, at a depth of ≈10 μm, a significant change in the FWHM was observed, and a somewhat smaller shift was detected in the peak position. According to TRIM investigations, these shifts are located at the approximate depth of the EOR of the implanted protons. The data for this series is presented in figure 47(b).

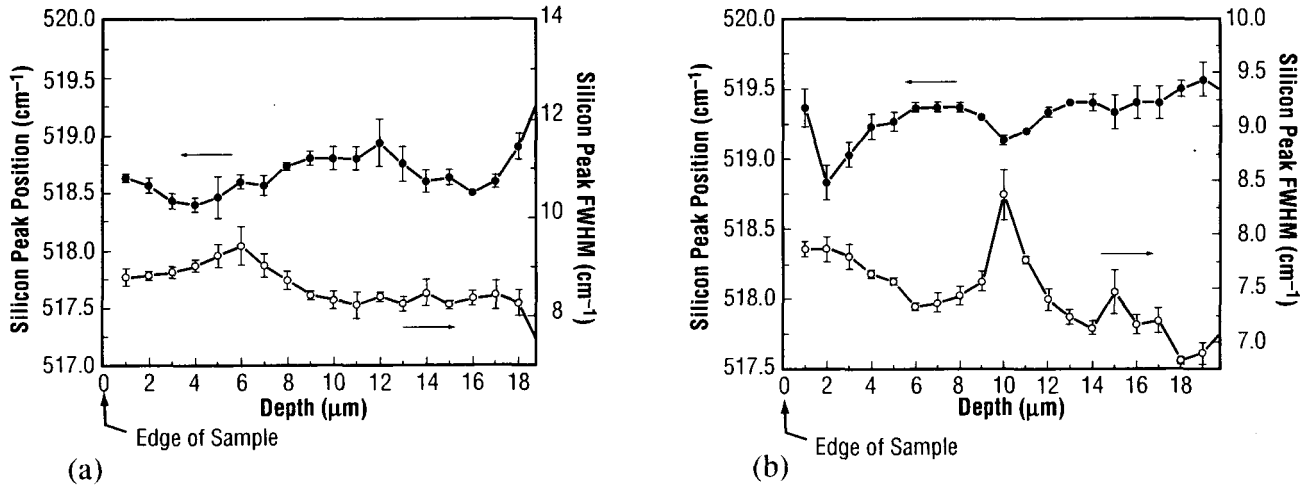

Figure 47. Micro-Raman spectra as a function of depth across: (a) The cleaved surface of the as-deposited polycrystalline silicon film and (b) the 2×10^{15} H^+/cm^2-implanted polycrystalline silicon film.

The Raman data from the 2×10^{16} H^+/cm^2 implant followed the same trend observed in the two previous specimens and is shown in figure 48(a). Scatter was observed in the silicon peak position throughout the depth of the film. A change in the FWHM as a function of depth is also evident near the EOR. There is a great deal of variability within the data points in this depth range that was not observed in most other regions of the film.

The Raman data from the most heavily implanted polycrystalline silicon film are presented in figure 48(b). The peak position as a function of depth is observed to be shifted slightly downward throughout the entire implanted region, especially near the EOR, and the downward shift appears to extend a couple of microns past the EOR. When factoring in the experimental error, the FWHM also follows this trend, but not to the same degree as the peak-position shift.

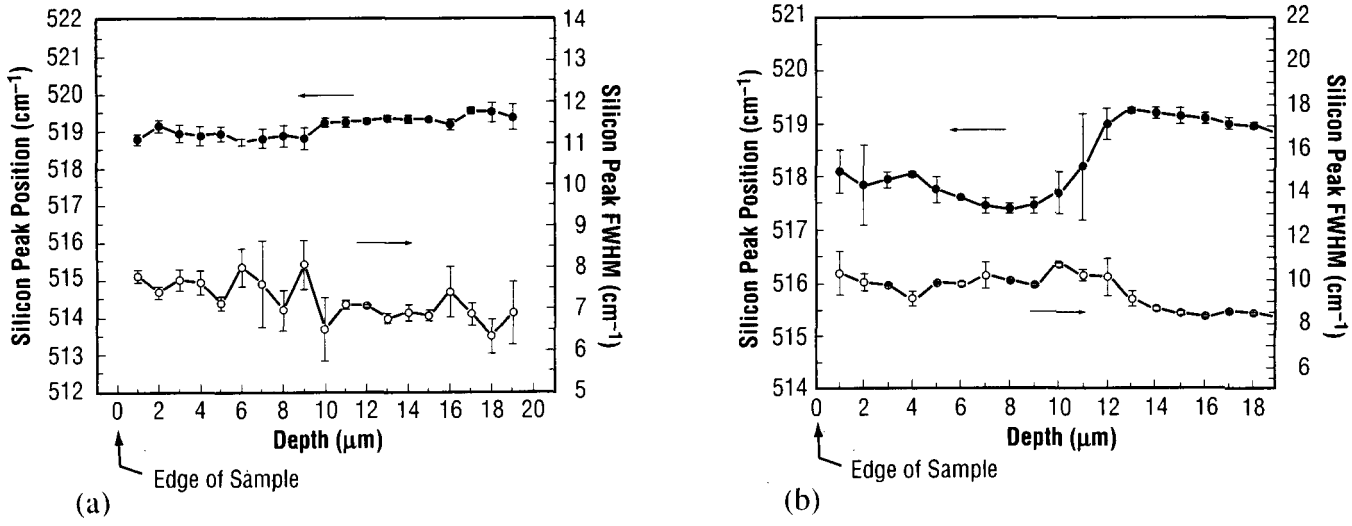

Figure 48. Micro-Raman spectra as a function of depth across the cleaved surface of: (a) The 2×10^{16} H^+/cm^2-implanted polycrystalline silicon film and (b) the 2×10^{17} H^+/cm^2-implanted polycrystalline silicon film.

Figure 49(a) presents the variation in peak position as a function of depth for the entire silicon series. A high degree of variability is observed in the data set, not only in the regions that received the proton implantation but also in the nonirradiated regions. As already discussed, this can be attributed to the irregularities within the film itself and irregular edges on the cleaved surfaces that result in non-uniform focusing of the laser on the surface of the specimens. The most heavily irradiated specimen, the 2×10^{17} H^+/cm^2 implant, appears to have a significantly shifted peak position when compared to the film past the EOR and the other implant series.

A similar chart, showing the variation in FWHM as a function of depth for the entire series, is presented in figure 49(b). Once again, a large amount of variation in each implant and in the entire series is evident. The most heavily irradiated specimen appears to show a trend of increasing FWHM until reaching a maximum at a depth of 10 μm. The data failed to converge to a consistent baseline in the nonirradiated regions of the films even though all four specimens were randomly selected from one wafer.

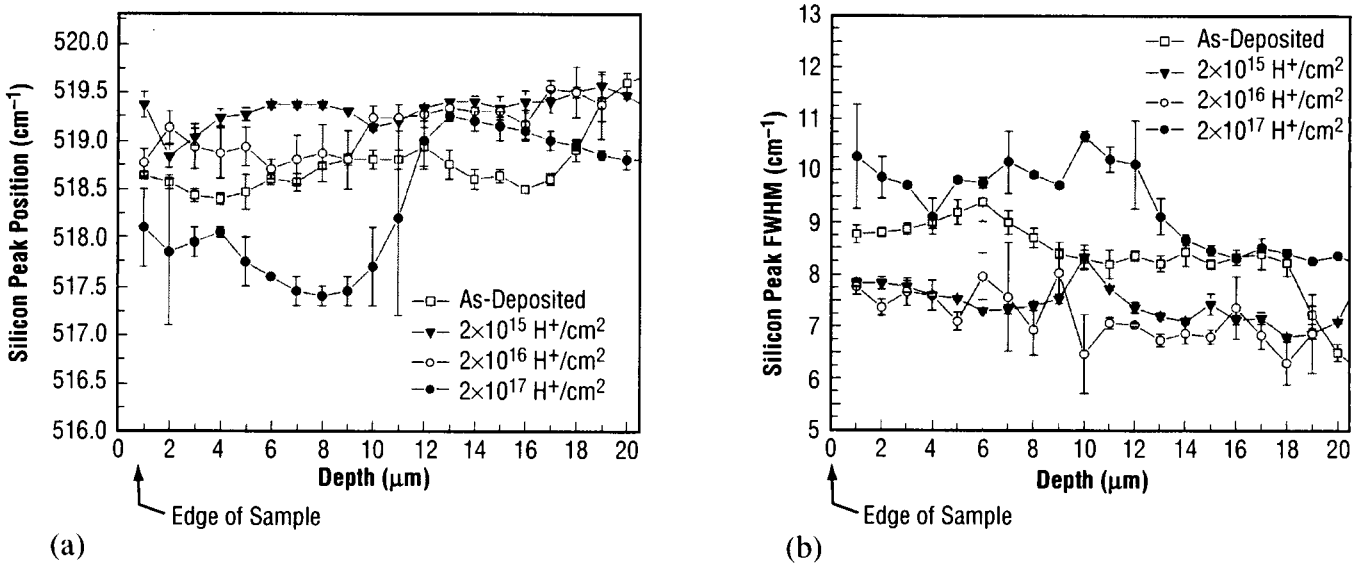

Figure 49. Summary chart for the entire polycrystalline silicon implantation series showing the variation in: (a) Peak position as a function of depth and (b) FWHM as a function of depth.

4.10 Micro-X-Ray Diffraction

The most heavily irradiated diamond specimen, the 2×10^{17} H^+/cm^2 implant, was examined in detail via depth-resolved micro-XRD. This specimen was examined at six different locations on the top surface. Both normal strain and shear strain were investigated. Figure 50 is a representative plot of the normal strain components as a function of depth for one of the six locations investigated. Within the range of the proton implantation, the deviatoric strain tensor is positive for the ε_{xx} component, slightly positive for the ε_{yy} component, but somewhat negative for the ε_{zz} component. Past the EOR, the components return to much lower values and remain fairly constant throughout the depth of the film. The normal strain component ε_{xx} showed the least amount of fluctuation throughout the depth of the film.

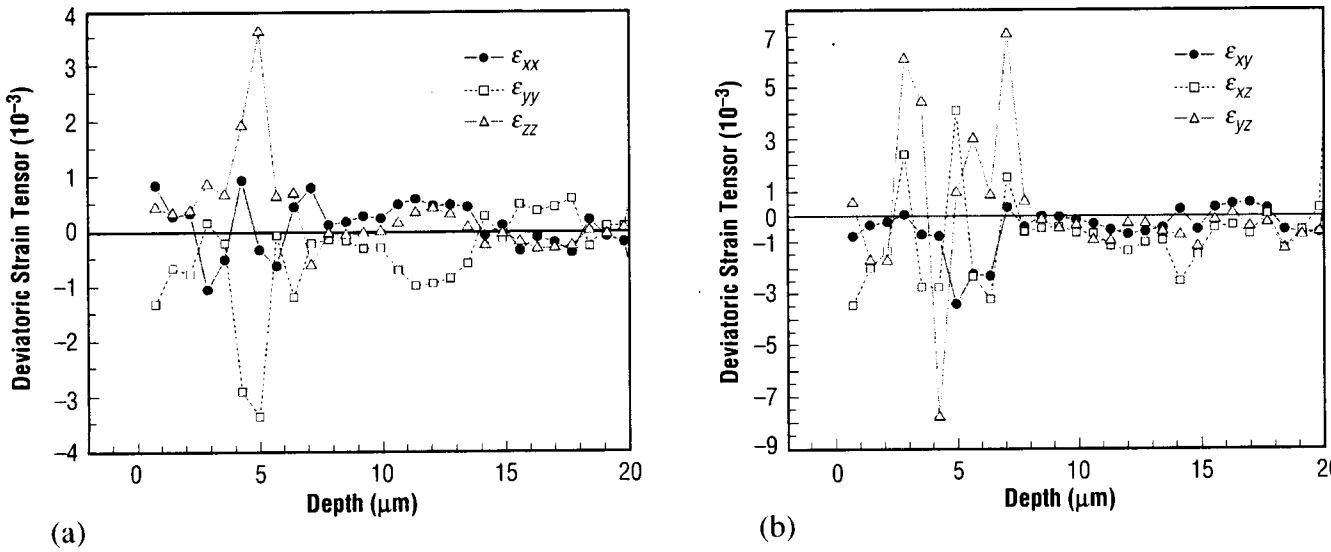

Figure 50. Components as a function of depth for the deviatoric strain tensor for the 2×10^{17} H^+/cm^2-implanted diamond specimen for: (a) Normal components and (b) shear components.

Examination of the shear component of the strain tensor indicates large fluctuations for all three components, ε_{xy}, ε_{xz}, and ε_{yz} until reaching a depth of ≈8 μm (fig. 50(b)). Past this depth, all three components return to a very low and consistent value until reaching the end of the film. Unlike the normal strain, the values for ε_{xy} undulate widely from positive to negative from one micron to the next. This is also observed, but to a lesser degree, in the ε_{xz} component. In both the normal and shear components, the values of the deviatoric strain tensors are on the scale of 10^{-3}. During data collection, the x-ray microprobe intersected six different grains from the free surface to the silicon substrate—a distance of roughly 20 μm.

5. DISCUSSION

In this section, an analysis is undertaken to examine how well theoretical proton implantation modeling compares to the observed experimental results. Strain values are calculated using both the Raman and XRD techniques, and the microstructure of the irradiated specimens near the EOR is examined. Finally, the behavior of the silicon specimens is examined.

5.1 Implantation Modeling—Diamond

TRIM calculates damage; i.e., vacancies, interstitials, and knock-on atoms, as a function of implantation depth in a material. The cross-sectional sample configuration used throughout these experiments provided optimum conditions for theoretical and experimental comparisons. The 2×10^{17} H^+/cm^2 implant showed a significant shift in first-order diamond peak position and FWHM. Due to the fact that the diamond line shape was symmetrical rather than skewed, the defects were considered to be localized in the form of point defects. Surface damage was greater than that which was predicted using TRIM analysis, which failed to predict nuclear; i.e., microstructural, damage near the surface. This omission is consistent with other ion implantation studies using heavier ions with diamond material, mainly mono-crystalline, in which surface damage was observed but not predicted using TRIM software. This study shows that unpredicted surface damage is the case using light ions, such as protons, in polycrystalline diamond films as well.

The main reasons that TRIM underestimates surface damage are that it does not account for dynamic annealing, defect diffusion, or the effects of gradual damage accumulation. Examination of the 2×10^{17} H^+/cm^2 series at the 1-μm depth provides additional support for defect-related surface damage. In addition to the spectra containing graphitic-like components at ≈1,580 cm^{-1}, defect-related damage was also present at 1,495 and 1,630 cm^{-1}. The FWHM of the top surface of the 2×10^{16} H^+/cm^2 sample also indicated defect-related damage, evidenced by the 1,630-cm^{-1} peak. No surface damage was observed for the as-deposited and 2×10^{15} H^+/cm^2-implanted specimens.

Within the experimental error of ≈1 μm and given the spatial resolution of the Raman measurements, TRIM accurately predicted the maximum depth that the implanted protons would penetrate into the diamond films. The peak shift and FWHM increase rapidly for both the 2×10^{16} H^+/cm^2- and 2×10^{17} H^+/cm^2-implanted series until reaching a maximum at ≈4 μm. At this depth, the main Raman features are the 1,630-cm^{-1} split interstitial and a shifted, attenuated, and broadened first-order diamond peak. While the EOR region is very narrow, ≈0.5 μm, the first-order diamond peak does not return to baseline until ≈6 μm beyond the implant region.

This unexpected slow return to baseline has been observed in a prior study of ^{13}C-implanted natural type diamond. Spits et al. observed a similar tailing behavior by using the resonant nuclear reaction ^{13}C 9p, gamma ^{14}N at 550 keV.[31] They discovered that the depth to which the tail penetrates appears to be temperature dependent and the lower the temperature, the greater the penetration. They

concluded that interstitials are forced out of the implanted area, under high strain, and into the bulk. In the present study, the presence of grain boundaries in the material apparently did not serve as a barrier to this carbon interstitial migration.

To further illustrate this slow return to baseline, a comparison was made of the present experimental data and a study by Jamieson et al. (fig. 51) in which helium ions were implanted into monocrystalline diamond using megaelectronvolt energies.[32] It is important to note that a straightforward comparison is not possible since different ions, energies, implantation energies, etc. were used in the two studies. However, the behavior past the EOR is quite different in the two materials.

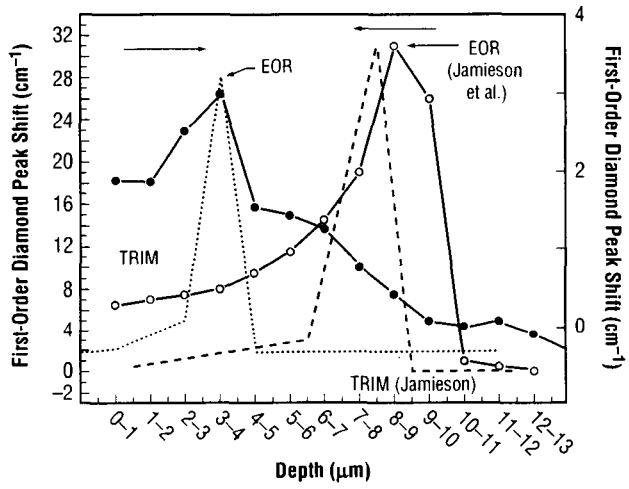

Figure 51. Comparison of depth-dependent Raman analysis as a function of depth for helium ion implantation into single-crystal diamond (solid dots and dotted line) as opposed to proton implantation into polycrystalline diamond (hollow dots and dashed line).

5.2 Hydrostatic Strain Calculations via Raman Spectroscopy—Diamond

Raman spectra of diamond films are greatly affected by stress and strain. In the absence of strain, the first-order Raman signal consists of a single, sharp peak. In the presence of hydrostatic strain, this peak shifts. In the presence of anisotropic strain, the crystal symmetry is altered, which results in a split of the Raman line. The degree of shift or splitting of the Raman spectra depends on the magnitude of the stress. A variety of previous studies have examined stress and strain values of polycrystalline diamond films deposited on various substrates.[33–35] The biaxial strain in a diamond film can be obtained by the use of the equation

$$\varepsilon = -5.64 \times 10^{-4} \text{ cm} \left(\nu_s - \nu_o\right) , \tag{1}$$

where ν_o is the position of the diamond peak for unstressed diamond, and ν_s is the corresponding position in a diamond film with a biaxial stress. Equation (1) is a weighed average, based on the singlet and doublet peaks observed in a biaxially strained diamond film. As figure 52 illustrates, first-order Raman

peak separation did not occur for the samples examined in this study, thus, this calculated strain value is for the hydrostatic component of the strain tensor. This spectra is from the most heavily irradiated material, the 2×10^{17} H^+/cm^2 implant, shown at the maximum depth of ion-implanted damage, ≈4 μm from the top surface.

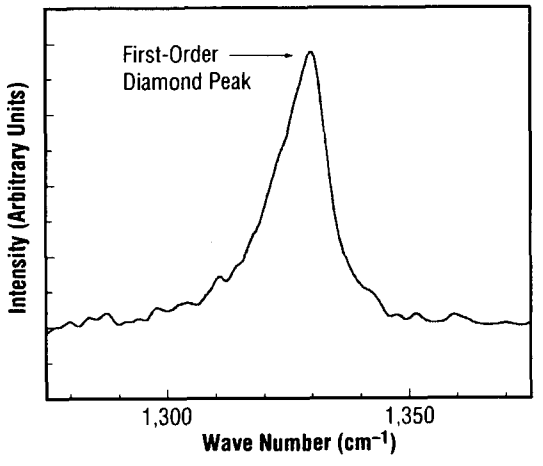

Figure 52. First-order diamond peak of 2×10^{17} H^+/cm^2-implanted diamond. While the peak is broad, skewed, and shifted downward, peak splitting is not observed.

Using equation (1), the strain values for both the 2×10^{16} H^+/cm^2- and 2×10^{17} H^+/cm^2-implanted specimens were calculated and are shown in figure 53. In the 2×10^{16} H^+/cm^2 specimen, the strain value reaches a maximum of 0.0009 at 4 μm. It returns to baseline levels just past the 8 μm location.

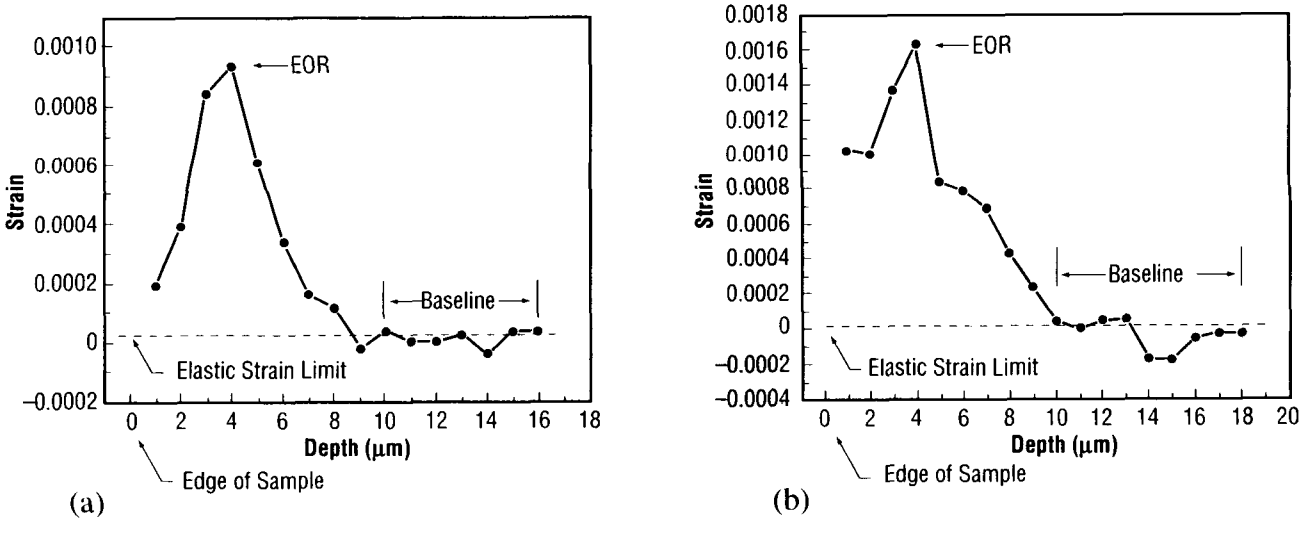

Figure 53. Calculated elastic strain as a function of depth for: (a) The 2×10^{16} H^+/cm^2-implanted diamond specimen—the elastic strain limit for certain diamond-based MEMS devices is exceeded in the first 8 μm of the film, and (b) the 2×10^{17} H^+/cm^2-implanted diamond specimen—elastic strain limit for certain diamond-based MEMS devices is exceeded in the first 10 μm of the film.

The most heavily irradiated specimen, 2×10^{17} H^+/cm^2, follows a similar trend, reaching a maximum of 0.0016 at 4 μm and returning to baseline at a depth of ≈10 μm. It should be noted that while the 2×10^{17} H^+/cm^2 sample received 10 times the dose of protons, the strain levels were only twice the value as in the 2×10^{16} H^+/cm^2 sample. This can be attributed, in part, to the resistance of the diamond lattice to distortion of the sp^3 hybrid bonding.[36]

While the strain values of the 2×10^{16} H^+/cm^2- and 2×10^{17} H^+/cm^2-implanted specimens exceeded the maximum value that would be allowable for certain diamond-based MEMS applications, the results indicate that, overall, the films contain a very low amount of strain.

5.3 Deviatoric Strain Calculations via Micro-X-Ray Diffraction—Diamond

The deviatoric strain component of the strain tensor was measured using the micro-XRD system. The strain tensor can be written in terms of both the hydrostatic (dilation) and distortion (deviatoric) components. The equation is

$$\varepsilon = \begin{pmatrix} \varepsilon 11 - \frac{\Delta}{3} & \varepsilon 12 & \varepsilon 13 \\ \varepsilon 12 & \varepsilon 22 - \frac{\Delta}{3} & \varepsilon 23 \\ \varepsilon 13 & \varepsilon 23 & \varepsilon 33 - \frac{\Delta}{3} \end{pmatrix} + \begin{pmatrix} \frac{\Delta}{3} & 0 & 0 \\ 0 & \frac{\Delta}{3} & 0 \\ 0 & 0 & \frac{\Delta}{3} \end{pmatrix}, \tag{2}$$

where $\Delta = \varepsilon 11 + \varepsilon 22 + \varepsilon 33$. The first term is called the deviatoric strain term, and the second term is the dilatational strain term.[37] As shown earlier, the normal and shear components vary greatly as a function of film depth, but the relative values of the tensor are extremely small, $\approx 10^{-3}$. One of the contributing factors for such variation as a function of depth can be explained by noting that this material is polycrystalline (shown schematically in fig. 54).

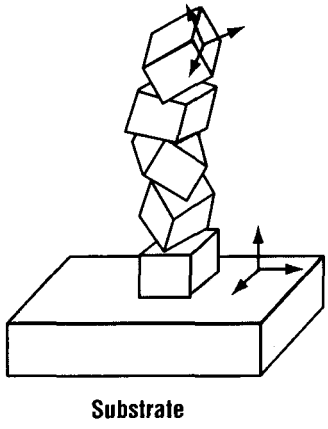

Figure 54. In the polycrystalline state, the crystallites are randomly oriented in three dimensions.[38]

As a polycrystalline material, the grains are randomly oriented, although some degree of columnar growth was observed in the SEM examination. Since submicron diffraction analysis measures lattice parameters directly, submicron diffraction analysis of the strains would be expected to vary as a function of location in the material due to grain boundaries and defects present in the film. The small increase in the values near the implanted region, due to the <100> split interstitials, indicate that the ion implantation is contained within a very narrow region. As a function of depth, the shear components quickly change from tensile to compression. This change may be attributed to the fact that the <111> direction is the preferred slip direction in diamond and may introduce shear into the crystal. In this case, however, sampling methodology is likely contributing to these fluctuations in the shear data because the strain measurements greatly depend on peak-position fitting and beam optics calibration. As a result, the normal shear components are less sensitive to sample stability during measurement, beam intensity fluctuations, etc., and should be considered more representative of the actual stress states within the films. These micro-XRD results are preliminary and more indepth analysis will be required to conclusively determine the microstrain fields that are associated with implanted polycrystalline diamond.

5.4 Additional Strain Analysis

Both the Raman and XRD techniques indicate that ion implantation creates tension inside the diamond lattice. Theoretical calculations of the ideal strength of diamond provide insight into the stability of diamond. Roundy and Cohen have calculated these values for diamond along the <111> direction.[39] In their work, they discovered that the properties of diamond under strain are dominated by the stability of the graphite structure, which high implantation/annealing creates. In shear, the ideal strength of diamond is 93 GPa with a critical strain of 0.3. In tension, the ideal strength is 95 GPa, but the critical strain is reduced to 0.13. The shear and tension values are shown graphically in figure 55. The end result is that the ion implantation process creates a situation in which the critical strain to convert to graphite is greatly diminished.

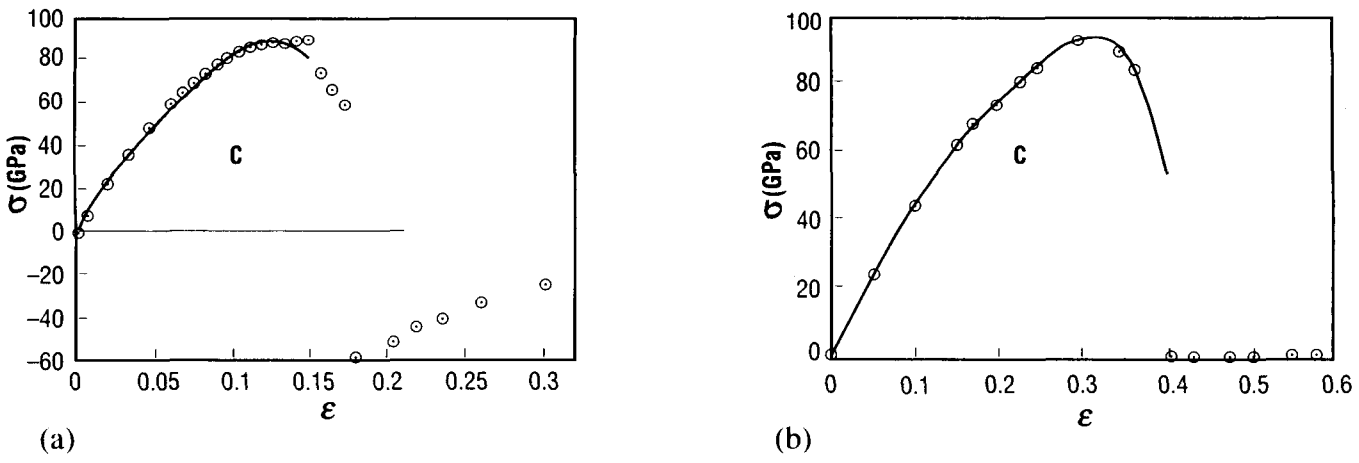

Figure 55. Diamond values for: (a) Tension and shear and (b) stress and strain. The critical value of strain for the transition from diamond to graphite is greatly diminished in the tension configuration.

Based on the experimental results in the present study, the strain values in the films near the region where the diamond-to-graphite transition is expected to occur are very low. This is true for even the most heavily irradiated specimen.

5.5 Phase Transition Thresholds—Diamond

The irradiation dose at which crystalline diamond converts to the more thermodynamically stable graphite structure is the subject of ongoing research. Based on the work of Uzan-Saguy et al., a dose level for this study was chosen that should have resulted in the diamond near the EOR becoming amorphous.[40] There should be a region between 3 and 4 μm in depth where the diamond should have become amorphous; however, the cross-sectional micro-Raman analysis of the region that received the dose, which should have created this damaged zone, did not indicate such a change. The diamond peak at the EOR was still clearly present albeit red-shifted, greatly diminished in intensity, and possessing a large FWHM. However, the authors did mention that the fact that the portions of the TRIM profiles used to deduce the critical damage density and the corresponding implant concentrations at the graphite/diamond interface are on the steep trails of the distributions results in rather large uncertainties in determining the critical dose. Also, it is possible that an amorphous layer was created but that the spatial resolution of the Raman system precluded its detection. However, that is unlikely because many spectra were obtained in this region. All of the spectra possessed the characteristic first-order diamond peak.

An important difference between their work and the present study deals with the fact that they examined monocrystalline diamond rather than polycrystalline material. However, others have implanted polycrystalline diamond past the critical dose value and failed to see the conversion of the diamond to graphite. Wang et al. implanted CVD diamond films with boron with a dose of 4×10^{15} to 5×10^{15} B^+/cm^2 and found the crystalline structure of the diamond was retained even after annealing, as opposed to others that had implanted similar dosages into single-crystal diamond and observed that the material became amorphous.[41] Wang suggested that the grain boundaries in the diamond films may be more apt to allowing relaxation of the lattice during irradiation.

Based on the large tail observed in the Raman data for both the 2×10^{16} H^+/cm^2 and 2×10^{17} H^+/cm^2 implants, some interstitials created by the proton implantation might have migrated to deeper layers of the diamond film. If strain was the cause, it is surprising that such a relatively small strain could cause the ejection of carbon atoms to deeper layers of the film. If, as proposed by Wang, grain boundaries allow for less microstructural damage to implanted regions in CVD diamond films, then the mechanism that might prevent implanted regions from becoming amorphous could possibly be responsible for assisting in interstitial migration due to the interstitials traveling along the grain boundaries. This could be an undesirable side effect of doping diamond films. The fact that no split interstitial or vacancy Raman signatures were detected in the tail regions indicate that the migrating species were neither of the two prominent ion-induced defect structures nor, for that matter, Raman active entities within the bandwidth examined.

5.6 Implantation Modeling and Raman Experimental Results—Silicon

Based on the Raman analysis of the top surfaces of the polycrystalline silicon specimens, little trace of implantation damage can be found. It is only in the most heavily irradiated specimen, the

2×10^{17} H^+/cm^2 implant, that significant shifts in the peak location and FWHM are observed. However, the drastically modified surface color of this specimen clearly demonstrated that the material had been altered by the implantation process.

In the cross-sectional SEM micrograph of the 2×10^{17} H^+/cm^2 implant, the presence of a distinct interface ≈8 μm from the surface corresponds well with the TRIM predicted EOR of 7.8 μm. While the experimental parameters selected for this research were done in order to study diamond in a radiation environment, performing analogous proton implantation on polycrystalline silicon at the highest dose used in these investigations was, in effect, mimicking some parts of a process known as smart-cut™.

Briefly, the smart-cut process is a layer-splitting technique that allows for an economical method of transferring thin surface layers from bulk substrates onto a host of other substrates. This process is used in the production of silicon-on-insulator materials, although the implant energy used in the present studies exceed those normally employed. Hochbauer et al. have studied this process in great detail. Using Rutherford backscattering spectroscopy, electron recoil detection, and high-resolution transmission electron microscopy methods, they have determined that implanted protons are trapped in the silicon lattice, once again in the BC location.[42]

While micro-Raman investigations into proton implantation in single-crystal silicon have been studied,[43,44] a search of the literature found no information about cross-sectional micro-Raman spectroscopy of proton-irradiated polycrystalline silicon films. The large variations in the data for the silicon series precluded meaningful strain calculations. The highest implant dosage used in this investigation created a buried interface that would likely compromise the structural integrity of a MEMS-based device.

6. CONCLUSIONS AND FUTURE WORK

The main objective of this research was to examine the effects of proton irradiation on the micro-structural properties of CVD diamond and polysilicon films. This information is needed since CVD diamond may find use as a structural material in space-based MEMS devices, and CVD diamond's response to radiation needs characterization. Prior to this investigation, polycrystalline diamond films had never been heavily irradiated with protons and then examined as a function of depth using micro-Raman and micro-XRD techniques. Micro-Raman analysis of polycrystalline silicon was also examined along side of the diamond films for comparison purposes.

The depth-dependent micro-Raman spectra for the as-deposited diamond film demonstrate the efficacy of film fabrication using the MPACVD method. Near the surface, small amounts of graphitic carbon were detected; however, this is to be expected as a result of film growth termination. At all remaining depths, the diamond was devoid of graphitic carbon. The first-order diamond peak was intense and stress free. Even near the silicon substrate, the diamond shows little degradation in quality.

Three different diamond films were implanted with varying doses of protons in an accelerator. This was done to simulate a space-based radiation environment. While the larger dosages were known to exceed the amount of radiation expected during a normal operational lifetime for a device, they were performed in an attempt to initiate the diamond-to-graphite conversion, and thus, examine the region around this phenomenon microstructurally. Implant dosages were chosen based on several prior studies, which indicated that above a defect concentration of 10^{22} defects/cm^3 the diamond would become amorphous.

After implantation, a visual inspection of the films revealed a noticeable darkening of the two more highly implanted specimens, the 2×10^{16} H^+/cm^2 and 2×10^{17} H^+/cm^2 implants. SEM analysis of the top surface showed a small amount of darkening in some locations in the 2×10^{16} H^+/cm^2-implanted films with extensive surface damage and heavy discoloration of the 2×10^{17} H^+/cm^2 films. Cross-sectional SEM analysis of the specimens failed to reveal any obvious effects of the implantation at any depth.

Much information was collected from the Raman data. Due to the downward shift in the first-order diamond peak, the 2×10^{16} H^+/cm^2- and 2×10^{17} H^+/cm^2-implanted films were shown to be under tensile stress. This stress reached a maximum near the EOR of the protons $\approx$4 μm from the surface. The broadening of the peak correlated with the implant dosages, which indicated a high degree of micro-structural damage. This damage was confirmed by the presence of known ion implantation-related defects detected in the Raman spectra—mainly the vacancy and the <100> split interstitial. Strain measurements were then made on the films. Due to an absence of peak splitting, only the hydrostatic component was observable. The values were shown to be extremely low, less than 0.002. The strain values in the most heavily irradiated specimen were shown to be $\approx$2 times those of the next most heavily irradiated specimen, yet the implantation dosage was >10 times larger. This resistance to microstruture distortion is partly due to the extremely strong sp^3 bond present in diamond.

An interesting observation was noted in the Raman data. The stress created by the implantation process extended well into unirradiated material and did not return to a baseline until reaching a depth of ≈2×EOR. This observation has been noted before in monocrystalline diamond. The authors of that study concluded that high stress states in the implanted region forced interstitials into the bulk. In this study, the presence of grain boundaries did not appear to act as a barrier in preventing this interstitial migration.

While the first-order diamond peak was significantly diminished in the most heavily irradiated film, the diamond structure was not completely destroyed at any location in the film. This result is contrary to the majority of prior studies but is consistent with a small handful of other studies in which an implant dose that theoretically should have produced an amorphous region did not do so. Very recently, an alternative theory has been proposed concerning the dosage needed to create an amorphous region. The present study compared favorably with much of that theory.

In order to gain additional insight concerning the microstructural effects of proton implantation into diamond films, another experimental method with high spatial resolution was chosen, the recently developed micro-XRD technique. Using this technique, the deviatoric component of the strain tensor was measured as a function of depth for the 2×10^{17} H^+/cm^2-implanted specimen. Both the normal and shear components were evaluated. The normal component indicated a positive strain perpendicular to the surface at approximately the EOR. The creation of a large amount of <100> split-interstitial aggregates, which create a dilatory volume change in the region, could account for much of this observation. The slow return to baseline values past the EOR was not observed to the same degree as noted in the Raman analysis. Spatial sampling volume differences between the two methods could account for much of this discrepancy, especially in polycrystalline films. The calculated values for the strain tensors were on the order of 10^{-3}.

Since polycrystalline silicon is currently the material used most often in MEMS devices, parallel experimentation was conducted on irradiated silicon specimens as well. Visually, little change was observed in the silicon specimens except for the most heavily irradiated sample. The material turned a dark blue due to the heavy proton implantation. SEM analysis of the top surfaces failed to present any implantation artifacts. Due to how soft silicon is compared to diamond, the lack of implantation artifacts is not surprising; i.e., the protons passed through the top surface with little resistance. Cross-sectional SEM analysis failed to detect any radiation-induced changes, except in the most heavily implanted specimen. In this case, an interface is clearly visible ≈8 μm from the top. This location is near the EOR predicted by implant modeling software. This interface should have a significant and degratory impact on polysilicon when used for structural MEMS purposes.

Raman analysis of the top surface of the polysilicon films did indicate a slight amount of peak broadening and shifting to lower wavelengths. This again would be consistent with ion implantation-induced stress and defects that are present. The cross-sectional micro-Raman data was somewhat inconclusive. A slight amount of peak-position broadening and peak-position shifting was observed for the most heavily irradiated specimen. This correlated loosely with depth, but due to the high degree of disorder from grain to grain, also evidenced in the as-deposited film, detailed correlations of implantation effects with depth were not possible. Also for this reason, micro-XRD experiments were not deemed useful for this investigation.

This research demonstrates the challenges involved when attempting to experimentally measure material properties on the submicron scale. Even when seemingly complimentary techniques are available, integration of the data is challenging due, in large part, to spatial issues. The sampling volume of micro-XRD is much smaller than the sampling volume in micro-Raman. The net effect is that information from a single micro-Raman data point will more than likely contain contributions from both intergranular and intragranular components. Conversely, the micro-XRD data can fluctuate considerably from one data point to the next due to the contribution of grain boundaries and defects. An interesting experiment would be to couple advanced micro-Raman techniques that have even smaller spot size with micro-XRD experiments.[42] In this fashion, one could be assured that essentially the same three-dimensional location within the specimen is being sampled by both techniques.

In relation to diamond-based MEMS devices, future work in this area could include additional studies of the mechanism that created the stress fields past the EOR in diamond material. More study is needed concerning the parameters that affect the diamond-to-graphite transition, such as implant temperature, ion species, and dosages required. Also, amorphous diamond films, which are beginning to see uses in diamond-based MEMS devices, should be experimentally examined for radiation tolerance.

Based on the results presented herein, CVD diamond used for structural MEMS purposes should be able to withstand proton radiation dosages that far exceed those expected in near-Earth orbits. Polysilicon should also perform satisfactorily. A challenging investigation would be to construct a diamond-based MEMS device and observe the stress and strain in real time as a function of implantation dosage. This would be desirable so that a shift from static to dynamic studies of diamond thin films and the effects of irradiation could be made.

REFERENCES

1. Kant, A.; Drory, M.D.; Moody, W.J.; et al.: "Microstructural Effects on the Hardness, Elastic Modulus and Fracture Toughness of CVD Diamond," *MRS Symposium Proceedings*, Vol. 505, pp. 611–616, 1998.

2. Novikov, N.V.; and Dub, S.N.: "Hardness and Fracture Toughness of CVD Diamond Film," *Diamond and Related Materials*, Vol. 5, pp. 1,026–1,030, 1996.

3. Blank, V.; Popov, M.; Pivovarov, G.; et al.: "Mechanical Properties of Different Types of Diamonds," *Diamond and Related Materials*, Vol. 8, pp. 1,531–1,535, 1999.

4. Spearing, S.M.: "Material Issues in MEMS," *Acta Mater.*, Vol. 48, pp. 179–196, 2000.

5. Richter, A.; Ries, R.; Smith, R.; et al.: "Nanoindentation of Diamond, Graphite and C_{60} Films," *Diamond and Related Materials*, Vol. 9, pp. 170–184, 2000.

6. Ziegler, J.F.; Biersack, J.P.; and Littmark, U.: *The Stopping and Range of Ions in Matter*, p. 321, Pergamon Press, New York, NY, 1985.

7. Bushan, B.; and Koinkar, V.N.: "Microtribological Studies of Doped Single-Crystal and Polysilicon Films for MEMS Devices," *Sensors and Actuators*, Vol. 57, p. 91, 1996.

8. Michler, J.; Mermoux, M; Kaenel, Y.; et al.: "Residual Stress in Diamond Films," *Thin Solid Films*, Vol. 357, pp. 189–201, 1999.

9. Fan, Q.H.; Gracio, J; Pereira, E.; et al.: "Evaluation of Residual Stresses in Chemical Vapor Deposited Diamond Films," *J. Appl. Phys.*, Vol. 87, p. 2,880, 2000.

10. Steeds, J.W.; Charles, S.J.; Gilmore, A.C.; et al.: "Extended and Point Defects in Diamond Studied With the Aid of Various Forms of Microscopy," *Microscopy and Microanalysis*, Vol. 6, pp. 285–290, 2000.

11. Robinson, M.T.; and Torrens, I.M.: "Computer Simulation of Atomic-Displacement Cascades in Solids in the Binary-Collision Approximation," *Phys. Rev. B.*, Vol. 9, No. 12, p. 5,008, 1974.

12. Saada, D.; Adler, J; and Kalish, R.: "Transformation of the Diamond (sp^3) to Graphite (sp^2) bonds by Ion-Impact," *Int. J. Modern Phys. C*, Vol. 9, No. 1, p. 61, 1988.

13. Friedland, E.; and Sellschop, J.P.F.: "Temperature Dependence of Critical Damage Energies in Diamond," *Nucl. Instr. & Methods in Phys. Res. Sec. B*, Vol. 191, pp. 17–21, 2002.

14. Breuer S.J.; and Briddon, P.R.: "Ab Initio Investigation of the Native Defects in Diamond and Self-Diffusion," *Phys. Rev. B*, Vol. 51, No. 11, p. 6,984, 1995.

15. http://phycomp.technioni.ac.il/~david/thesis/node50.html, cited November 2001.

16. Duan, X.M.; Sun, D.Y.; and Gong, X.G.: "Hypermolecular Dynamic Simulations of Monovacancy Diffusion," *Compos. Mat. Sci.*, Vol. 20, No. 2, pp. 151–156, February 2001.

17. Coomer, B.J.; Resende, J.P.; Gross, R.; et al.: "The Divacancy in Silicon and Diamond," *Physica B*, Vol. 520, pp. 273–274, 1999.

18. Campbell, B.; and Mainwood, A.: "Radiation Damage of Diamond by Electron and Gamma Irradiation," *Physica Status Solidi (a)*, Vol. 181, pp. 99–107, 2000.

19. Fizgeer, B.; Uzan-Saguy, C.; Cytermann, V.; et al.: "Inhibition of Light Element Diffusion in Diamond Due to Ion Implantation Related Defects," *Physica Status Solidi (a)*, Vol. 186, No. 2, pp. 281–289, 2001.

20. Goss, J.P.; Jones, R.; Briddon, P.R.; et al.: "Theory of Hydrogen in Diamond," *Phys. Rev. B*, Vol. 65, 115,207, pp.1–13, 2002.

21. Machi, I.Z.; Buler, J.E.; Connell, S.H.; et al.: "Diffusion Characteristics of Hydrogen in Diamond," *Diamond and Related Materials*, Vol. 8, pp. 1,611–1,614, 1999.

22. Connell, S.H.; Sellschop, J.P.F.; Butler, J.E.; et al.: "A Study of the Mobility and Trapping of Minor Hydrogen Concentrations in Diamond in Three Dimensions Using Quantitative ERDA Microscopy," *Diamond and Related Materials*, Vol. 7, pp. 1,714–1,718, 1998.

23. Pickard, C.D.O.; Davis, T.J.; Wang, W.N.; et al.: *Diamond and Related Materials*, Vol. 7, pp. 238–242, February 1998.

24. Kalish, R.; Reznik, A.; Nugent, K.W.; et al.: "The Nature of Damage in Ion-Implanted and Annealed Diamond," *Nucl. Instru. & Methods in Phys. Res. Sec. B*, Vol. 148, pp. 626–633, 1999.

25. Durand, O.; Olivier, J.; Bisaro, R.; et al.: "Macroscopic Residual Stress in Chemical-Vapor-Deposition Free-Standing Diamond Films by X-Ray Diffraction Analyses," *Appl. Phys. Lett.*, Vol. 75, No. 13, pp. 1,881–1,883, September 27, 1999.

26. Mohrbacher, H.; Van Acker, K.; Blanpain, B.; et al.: "Diffraction and Micro-Raman Spectroscopy," *J. Mat. Res.*, Vol. 11, No. 7, pp. 1,776–1,782, July 1996.

27. Pandey, M.; D'Chunha, R.; and Tyagi, A.K.: "Defects in CVD Diamond: Raman and XRD Studies," *J. Alloys and Compounds*, Vol. 333, pp. 260–265, February 14, 2002.

28. Chung, J.-S.; and Ice, G.E.; "Automated Indexing for Texture and Strain Measurement With Broad-Bandpass X-Ray Microbeams," *J. Appl. Phys.*, Vol. 86, No. 9, p. 5,249, 1999.

29. Larson, B.C.; Yang, W.; Ice, B.E.; Dudal, J.D.; et al.: "Three-Dimensional X-Ray Structural Microscopy With Submicrometer Resolution," *Nature*, Vol. 415, pp. 887–890, 2002.

30. De Wolf, I.; Jian, C.; and van Spengen, M.W.: "The Investigation of Microsystems Using Raman Spectroscopy," *Optics and Lasers in Eng.*, Vol. 36, p. 213, 2001.

31. Spits, R.A.; Derry, T.E.; and Prins, J.F.: "Depth Profiling of Implanted ^{13}C in Diamond as a Function of Implantation Temperature," *Nucl. Instru. & Methods in Phys. Res. Sec. B*, Vol. 51, pp. 247–252, September 1990.

32. Jamieson, D.N.; Prauser, S; and Nugent, K.W.: "Cross-Sectional Raman Microscopy of MeV Implanted Diamond," *Nucl. Instru. & Methods in Phys. Res. Sec. B*, Vol. 106, pp. 641–645, December 1995.

33. Kuo, C.T.; Lin, C.R.; and Lien, H.M.: "Origins of the Residual Stress in the CVD Diamond Films," *Thin Solid Films*, Vol. 254, pp. 290–291, 1996.

34. Hollman, P.; Alahelisten, A.; Olsson, M.; et al.: " Young's Modulus and Fracture Stress of Hot Flame Deposited Diamond," *Thin Solid Films*, Vol. 270, pp. 137–142, 1995.

35. Fang, Z.; Xia, Y.; Wang, L.; et al.: "A New Quantitative Determination of Stress by Raman Spectroscopy in Diamond Grown on Alumina," *J. Phys.: Condensed Matter*, Vol. 14, p. 5,271, 2002.

36. Telling, R.H.; Pickard, C.J; Payne, M.C.; et al.: "The Theoretical Strength and Cleavage of Diamond," *Phys. Rev. Lett.*, Vol. 84, No. 22, pp. 5,160–5,163, 2000.

37. Chung, J.S.; and Ice, G.E.: "Automated Indexing for Texture and Strain Measurement With Broad-Bandpass X-Ray Microbeams," *J. Appl. Phys.*, Vol. 86, No. 9, pp. 5,249–5,255, 1999.

38. Anastassakis, E.; and Siakavellas, M.: "Elastic Properties of Textured Diamond and Silicon," *J. Appl. Phys.*, Vol. 90, No. 1, p. 144, 2001.

39. Roundy, D.; and Cohen, M.L.: "Ideal Strength of Diamond, Si, and Ge," *Phys. Rev. B*, Vol. 64, pp. 212,103–212,105 (3 pp.), 2001.

40. Uzan-Saguy, C.; Cytermann, C.; Brener, R.; et al.: "Damage Threshold for Ion-Beam Induced Graphitization of Diamond," *Appl. Phys. Lett.*, Vol. 67, No. 9, pp. 1,194–1,196, August 28, 1995.

41. Wang, J.; Yan, H.; Deng, Y; et al.: "The Comparative Study on Diamond Film by Near-Field Raman Spectroscopy and Micro-Raman Spectroscopy," *Solid State Communications*, Vol. 115, pp. 173–177, June 2000.

42. Hoechbauer, T.; Misra, A.; Verda, R.; et al.: "The Influence of Ion-Implantation Damage on Hydrogen-Induced Ion-Cut," *Nucl. Instru. & Methods in Phys. Res. Sec. B*, Vols. 175–177, pp.169–175, April, 2001.

43. Tyschenko, I.E.; Talochkin, A.B.; Kalesov, B.A.; et al.: "Raman and Photoluminescence Investigations of the H^+ Ion Implanted Silicon-on-Insulator Structure Formed by Hydrogen Ion Cut," *Nucl. Instru. & Methods in Phys. Res. Sec. B*, Vol. 186, pp. 329–333, January, 2002.

44. Galeazzo, E.; Salcedo, W.J.; Peres, H.E.; et al.: "Porous Silicon Patterned by Hydrogen Ion Implantation," *Sensors and Actuators B*, Vol. 76, pp. 343–346, 2001.

REPORT DOCUMENTATION PAGE

Form Approved
OMB No. 0704-0188

Public reporting burden for this collection of information is estimated to average 1 hour per response, including the time for reviewing instructions, searching existing data sources, gathering and maintaining the data needed, and completing and reviewing the collection of information. Send comments regarding this burden estimate or any other aspect of this collection of information, including suggestions for reducing this burden, to Washington Headquarters Services, Directorate for Information Operation and Reports, 1215 Jefferson Davis Highway, Suite 1204, Arlington, VA 22202-4302, and to the Office of Management and Budget, Paperwork Reduction Project (0704-0188), Washington, DC 20503

1. AGENCY USE ONLY *(Leave Blank)*	2. REPORT DATE	3. REPORT TYPE AND DATES COVERED
	August 2003	Technical Memorandum

4. TITLE AND SUBTITLE
Correlation of Radiation Dosage With Mechanical Properties of Thin Films

5. FUNDING NUMBERS

6. AUTHORS
R.L. Newton

7. PERFORMING ORGANIZATION NAMES(S) AND ADDRESS(ES)
George C. Marshall Space Flight Center
Marshall Space Flight Center, AL 35812

8. PERFORMING ORGANIZATION REPORT NUMBER
M–1088

9. SPONSORING/MONITORING AGENCY NAME(S) AND ADDRESS(ES)
National Aeronautics and Space Administration
Washington, DC 20546–0001

10. SPONSORING/MONITORING AGENCY REPORT NUMBER
NASA/TM—2003–212692

11. SUPPLEMENTARY NOTES
Prepared by the Materials, Processes, and Manufacturing Department, Engineering Directorate

12a. DISTRIBUTION/AVAILABILITY STATEMENT
Unclassified-Unlimited
Subject Category 33
Nonstandard Distribution

12b. DISTRIBUTION CODE

13. ABSTRACT *(Maximum 200 words)*
The objective of this investigation was to examine the relationship between irradiation level (proton dose), microstructure, and stress levels in chemical vapor deposited diamond and polysilicon films using cross-sectioned specimens. However, the emphasis was placed on the diamond specimen because diamond holds much promise for use in advanced technologies. The use of protons allows not only the study of the charged particle that may cause the most microstructural damage in Earth-orbit microelectromechanical systems (MEMS) devices, but also allows the study of relatively deeply buried damage inside the diamond material. Using protons allows these studies without having to resort to megaelectronvolt implant energies that may create extensive damage due to the high energy that is needed for the implantation process. Since MEMS devices operating in space will not have an opportunity to reverse radiation damage via annealing, only nonannealed specimens were investigated. The following three high spatial resolution techniques were used to examine these relationships: (1) Scanning electron microscopy, (2) micro-Raman spectroscopy, and (3) micro x-ray diffraction.

14. SUBJECT TERMS radiation, dosage, mechanical, thin films, chemical, vapor, correlation, crystal, diamond, graphite, silicon, implant, modeling, spectroscopy, micro-X-ray, proton

15. NUMBER OF PAGES
72

16. PRICE CODE

17. SECURITY CLASSIFICATION OF REPORT	18. SECURITY CLASSIFICATION OF THIS PAGE	19. SECURITY CLASSIFICATION OF ABSTRACT	20. LIMITATION OF ABSTRACT
Unclassified	Unclassified	Unclassified	Unlimited